



# Mass, morphing, metallicities: the evolution of infalling high velocity clouds

F Heitsch, A Marchal, M-A Miville-Deschênes, J Shull, A Fox

## ► To cite this version:

F Heitsch, A Marchal, M-A Miville-Deschênes, J Shull, A Fox. Mass, morphing, metallicities: the evolution of infalling high velocity clouds. Monthly Notices of the Royal Astronomical Society, 2022, 509 (3), pp.4515-4531. 10.1093/mnras/stab3266 . hal-03873379

**HAL Id: hal-03873379**

**<https://hal.science/hal-03873379>**

Submitted on 22 Mar 2023

**HAL** is a multi-disciplinary open access archive for the deposit and dissemination of scientific research documents, whether they are published or not. The documents may come from teaching and research institutions in France or abroad, or from public or private research centers.

L'archive ouverte pluridisciplinaire **HAL**, est destinée au dépôt et à la diffusion de documents scientifiques de niveau recherche, publiés ou non, émanant des établissements d'enseignement et de recherche français ou étrangers, des laboratoires publics ou privés.

# Mass, morphing, metallicities: the evolution of infalling high velocity clouds

F. Heitsch,<sup>1</sup>★ A. Marchal,<sup>2</sup> M.-A. Miville-Deschênes,<sup>3</sup> J. M. Shull<sup>4</sup> and A. J. Fox<sup>5</sup>

<sup>1</sup>*Department of Physics and Astronomy, University of North Carolina Chapel Hill, Chapel Hill, NC 27599, USA*

<sup>2</sup>*Canadian Institute for Theoretical Astrophysics, University of Toronto, Toronto ON M5S 3H8, Canada*

<sup>3</sup>*Laboratoire AIM, CEA-Saclay, CNRS, Université Paris-Saclay, Université Paris Diderot, Sorbonne Paris Cité, F-91191 Gif-sur-Yvette, France*

<sup>4</sup>*CASA, Department of Astrophysical and Planetary Sciences, University of Colorado Boulder, CO 80309, USA*

<sup>5</sup>*AURA for ESA, Space Telescope Science Institute, 3700 San Martin Drive, Baltimore, MD 21218, USA*

Accepted 2021 November 5. Received 2021 October 31; in original form 2021 July 30

## ABSTRACT

We revisit the reliability of metallicity estimates of high velocity clouds with the help of hydrodynamical simulations. We quantify the effect of accretion and viewing angle on metallicity estimates derived from absorption lines. Model parameters are chosen to provide strong lower limits on cloud contamination by ambient gas. Consistent with previous results, a cloud traveling through a stratified halo is contaminated by ambient material to the point that  $<10$  per cent of its mass in neutral hydrogen consists of original cloud material. Contamination progresses nearly linearly with time, and it increases from head to tail. Therefore, metallicity estimates will depend on the evolutionary state of the cloud, and on position. While metallicities change with time by more than a factor of 10, well beyond observational uncertainties, most lines-of-sight range only within those uncertainties at any given time over all positions. Metallicity estimates vary with the cloud's inclination angle within observational uncertainties. The cloud survives the infall through the halo because ambient gas continuously condenses and cools in the cloud's wake and thus appears in the neutral phase. Therefore, the cloud observed at any *fixed* time is not a well-defined structure *across* time, since material gets constantly replaced. The thermal phases of the cloud are largely determined by the ambient pressure. Internal cloud dynamics evolve from drag gradients caused by shear instabilities, to complex patterns due to ram-pressure shielding, leading to a peloton effect, in which initially lagging gas can catch up to and even overtake the head of the cloud.

**Key words:** Galaxy:halo – Galaxy:evolution – hydrodynamics – turbulence – methods:numerical.

## 1 BACKGROUND

The Galactic halo hosts a population of clouds whose line-of-sight velocities are inconsistent with Galactic rotation (Wakker & van Woerden 1997). Historically, identified by their neutral gas component observed via H I 21 cm emission, their mass budget is actually dominated by ionized gas (Fox et al. 2004; Shull et al. 2009; Lehner & Howk 2011). These high velocity clouds (HVCs) range from large complexes of many degrees to structures at the resolution limit. Their diversity suggests different origins (Wakker & van Woerden 1997; Putman, Peek & Jounge 2012).

HVC metallicities may provide key information about cloud origins. Metallicities range between 10 – 50 per cent solar (Wakker et al. 1999b; Fox et al. 2010; Shull et al. 2011; Richter et al. 2013; Collins, Shull & Giroux 2007; Richter 2017), possibly indicating satellite or circum-Galactic material as an origin. Intermediate and low velocity clouds (IVCs, LVCs) have higher metallicity, suggesting a Galactic wind source (Putman et al. 2012). Yet, mixing with or accretion of ambient material affects the reliability of metallicity constraints as indicators of HVC origin (Gritton, Shelton & Kwak

2014; Kwak, Shelton & Henley 2015; Armillotta, Fraternali & Marinacci 2016; Fox et al. 2016; Henley, Gritton & Shelton 2017).

The contamination problem is one of turbulent mixing (Esquivel et al. 2006; Kwak & Shelton 2010). Yet, turbulent mixing is a challenging problem, especially in inviscid hydrodynamic simulations. Convergence is hard to reach, and mixing can be dominated by the numerical scheme (Shin, Stone & Snyder 2008; Goodson et al. 2017) and by the physics included in the modelling (Vietri, Ferrara & Miniati 1997; Vieser & Hensler 2007a; McCourt et al. 2015; Sander & Hensler 2021). More recently, the focus has shifted to contamination by accretion relying on cooling. A sizeable fraction of the HVC population may be Galactic fountain material (Fraternali et al. 2015; Marasco & Fraternali 2017, see also Putman et al. 2012). Gas launched from the disc generates a wake, leading to condensation of halo gas due to radiative losses (Gronke & Oh 2020, see also Heitsch & Putman 2009). Up to 100 per cent of the original cloud mass may be accreted from the ambient gas (Gritton, Shelton & Galyardt 2017).

Best suited as a laboratory for HVCs are the Smith cloud (Smith 1963; Bland-Hawthorn et al. 1998; Lockman et al. 2008) and Complex C (Hulsbosch & Raimond 1966). Distances and orientations are well constrained (Wakker et al. 2003; Putman et al. 2003; Lockman et al. 2008 for the Smith Cloud; Wakker et al. 2007; Thom et al. 2008 for Complex C), to the point that trajectory reconstructions

★ E-mail: fheitsch@unc.edu

have been attempted (Nichols et al. 2014; Fraternali et al. 2015). Henley et al. (2017) compare their simulation results with the Smith Cloud, exploring different evolution times and viewing angles. They conclude that the probability to find ‘original’ cloud material decreases with distance from the leading head of the cloud, and that therefore the origin of the Smith Cloud remains uncertain.

We revisit the contamination scenario, focusing on the probability to identify original cloud material in the neutral gas phase. Our analysis differs in four aspects from Henley et al. (2017): (1) Instead of a wind-tunnel experiment, the cloud is dropped in a Galactic gravitational potential; (2) The analysis of ‘original’ cloud content is generalized to arbitrary viewing angles; (3) Column densities for metallicities are derived from line ratios, which in turn are determined by a Gaussian decomposition of the emission and absorption line profiles using ROHSA (Marchal et al. 2019); (4) We allow the gas to cool below  $10^4$  K. Radiative losses at  $10^5$  K already lead to cooling-induced fragmentation (Shull & Moss 2020). Cooling below  $10^4$  K can lead to the formation of cold neutral gas via thermal instability (Field 1965; Wolfire et al. 1995a, b), and thus can enhance overall fragmentation of the cloud (Tanner, Cecil & Heitsch 2016, for this effect on Galactic wind models).

We generated a set of hydrodynamic models of HVCs traveling through a diffuse halo medium (Section 2). We assess the probability to find cloud material at arbitrary positions (Section 3.2) and estimate the effects of contamination and viewing angle on abundance estimates (Section 3.4). We explore correlations between centroid velocities and metallicities (Section 3.5) and between column densities and metallicities (Section 3.6) as indicators for contamination. Caveats and consequences for observational estimates are mentioned in Section 4.

## 2 MODEL DESCRIPTION

We use a modified (Appendix A) version of Athena 4.2 (Stone et al. 2008), an Eulerian (fixed) grid code solving the equations of inviscid, compressible hydrodynamics in conservative form

$$\frac{\partial \rho}{\partial t} + \nabla \cdot (\rho \mathbf{u}) = 0, \quad (1)$$

$$\frac{\partial \rho C_c}{\partial t} + \nabla \cdot (\rho C_c \mathbf{u}) = 0, \quad (2)$$

$$\frac{\partial \rho C_h}{\partial t} + \nabla \cdot (\rho C_h \mathbf{u}) = 0, \quad (3)$$

$$\frac{\partial \rho \mathbf{u}}{\partial t} + \nabla \cdot (\rho \mathbf{u} \mathbf{u} + P) = -\rho \nabla \Phi, \quad (4)$$

$$\frac{\partial E}{\partial t} + \nabla \cdot ((E + P) \mathbf{u}) = \rho \mathcal{L}, \quad (5)$$

with the total mass density  $\rho$ , the gas velocity  $\mathbf{u}$ , the pressure  $P$  and the total energy

$$E \equiv \frac{1}{2} \rho \mathbf{u}^2 + \frac{P}{\gamma - 1}. \quad (6)$$

The ‘dye’ for the cloud ( $C_c$ ) [the halo ( $C_h$ )] is initialized to 1 wherever there is cloud [halo] material, and to 0 elsewhere. The adiabatic exponent is set to  $\gamma = 5/3$ , and the mean molecular weight to  $\mu = 1$  in units of  $m_H$ . The latter choice affects cloud masses and sound speeds. Therefore, we will quote mass ratios and any time-scales are approximations. The effective equation of state is determined by a combination of heating and cooling processes  $\mathcal{L}$  (Section A4) applied to the total energy equation (equation 5). We use the HLLC solver (Toro, Spruce & Speares 1994) in combination with a third-order Runge–Kutta integrator (Section A3).

## 2.1 Initial and boundary conditions

Not much is known about the ‘initial’ shape and structure of HVCs, if such a concept is valid at all. A popular choice is to assume a spherical cloud with some density and temperature profile (e.g. Quilis & Moore 2001; Vieser & Hensler 2007a; Heitsch & Putman 2009; Gritton et al. 2014; Sander & Hensler 2021, but see Cooper et al. 2009, though in a different context), which is then exposed to a wind, or, in our case, is falling through the Galactic halo. Such a set-up emphasizes the cloud survival aspect of a HVC simulation. This is not surprising, since many previous studies using such initial conditions were interested in the survival of original cloud material.

We approach the choice of initial conditions differently, since uniform-density initial conditions can leave a clear imprint on the cloud structure for a substantial time (Henley et al. 2017). We do not aim at setting up a realistic cloud in the initial conditions, but we develop initial conditions that evolve into a realistic cloud, and take that cloud as our starting point for the analysis. The reader could think of this as a burn-in phase; the first half of the simulation ( $\sim 140$  Myr) is used to set up the cloud. During this phase, the cloud mostly preserves its initial structure and consists of original cloud material, with only minor contributions from ambient gas. Since we are considering an idealized numerical experiment investigating the contamination of a model cloud by ambient gas, it does not matter whether the cloud formed via stripping of gas from dwarf satellites (Nichols et al. 2011), via Galactic winds/outflows (Fraternali et al. 2015), or via any other scenario.

In this spirit, we imagine that the HVC starts its voyage at an initial distance of  $\sim 30$  kpc above the plane, providing the cloud with sufficient room to lose any imprint of the initial conditions. We encase the cloud in a simulation domain such that it rests in the lower eighth of the box. The box measures  $1 \times 1 \times 8$  kpc<sup>3</sup> with 256 cells along the short dimension. The box is three times as wide as the initial cloud diameter, which is resolved by 85 cells. This should suffice to capture the large-scale dynamics of the cloud in three dimensions (Pittard & Parkin 2016; Goodson et al. 2017). We set an initial cloud mass of  $M_c = 5 \times 10^6 M_\odot$ , comparable to that of Complex C (Thom et al. 2008, see also Wakker et al. 2007) or – depending on the distance estimate – the Smith Cloud (Bland-Hawthorn et al. 1998; Lockman et al. 2008). The latter authors arrive at a lower mass limit for H I of  $10^6 M_\odot$  based on a comparison of several distance estimates placing the cloud at  $12.4 \pm 1.3$  kpc. The cloud is chosen to be sufficiently massive so that some of its neutral gas survives the passage through the halo (Heitsch & Putman 2009). The *initial*, average cloud density is  $n_H \approx 10 \text{ cm}^{-3}$ , or a factor of  $10^2$ – $10^3$  higher than the average HVC density for Complex C (Thom et al. 2008; Shull et al. 2011). Once we start the analysis, peak cloud densities have dropped to  $\sim 1 \text{ cm}^{-3}$ , with average densities of  $\sim 0.1 \text{ cm}^{-3}$ .

The cloud itself is realized via a double top-hat density profile, with temperatures corresponding to the two-phase equilibrium temperatures (see Section A4 for details on the thermal physics). We identify neutral gas (H I) via the ionization fraction  $x_i$  that is implicitly calculated as a function of total density  $n_{\text{tot}}$  in our thermal physics description. Thus, the neutral column density is  $N(\text{H I}) = \int n_{\text{tot}}(s)(1 - x_i(s))ds$  along a line of sight  $s$ . Initially at rest, the cloud does not have an ionized gas component, but this component will develop during the burn-in phase, reaching 50 per cent of the total cloud mass.

A fixed gravitational potential accelerates the cloud towards the disc. The potential consists of a combination of dark matter halo, spheroidal bulge and disc potentials (Strickland & Stevens 2000; Cooper et al. 2008; Tanner et al. 2016). We assume a Galacto-centric radius of 8.5 kpc, compared to 7.6 kpc for the Smith Cloud (Lockman

et al. 2008). For simplicity regarding boundary conditions, we let the cloud drop perpendicularly to the Galactic plane. We do not assume a dark matter halo confining the cloud (Quilis & Moore 2001; Nichols & Bland-Hawthorn 2009; Galyardt & Shelton 2016), nor do we include self-gravity (Sander & Hensler 2021).

We place the cloud in an initially isothermal, hydrostatically stratified halo determined by the gravitational potential, with  $T = 2.2 \times 10^6$  K (Gupta et al. 2012; Miller & Bregman 2013, 2015). Henley & Shelton (2014) discuss the justification for *non*-isothermal models, at lower temperatures. Our choice of an isothermal model is motivated by numerical considerations of stability. Non-isothermal models are prone to convection (Henley & Shelton 2014), and in combination with lower assumed temperatures (Wang & Yao 2012) would require additional mechanical heating mechanisms such as galactic winds or cosmic rays (Girichidis et al. 2016) to achieve the appropriate scale heights. The required densities ( $n \approx 10^{-4} \text{ cm}^{-3}$  at  $z = 30$  kpc) in our model halo are low enough that the cooling time is longer than the typical crossing time through the simulation box, and therefore, the ambient gas temperature does not change drastically as long as the gas is not perturbed by the cloud's passage. Lower halo temperatures would result in stronger cooling and thus in faster contamination of the cloud by ambient halo gas. We neglect any possible co-rotation of the warm halo gas with the Galactic disk (Qu et al. 2020). The cloud is initially in thermal pressure balance with the halo, at a pressure of  $P/k_B = 660 \text{ K cm}^{-3}$ . We apply a grid of velocity perturbations drawn from a turbulent spectrum with index  $|v|^2 \propto k^{-4}$  on a wavenumber range  $1/r_c \leq k \leq (2\Delta x)^{-1}$ , where  $r_c$  is the cloud radius. The specific choice of the turbulent spectrum does not affect the results. The velocity perturbations are normalized such that they generate a turbulent pressure  $\rho\sigma^2/k_B = 330 \text{ K cm}^{-3}$ , or 50 per cent of the thermal pressure. The velocity perturbations break the initial symmetry of the set-up, suppressing numerical artefacts typical for inviscid solvers in the presence of highly symmetric initial conditions. The kinetic energy from the turbulent motions make the cloud expand during the burn-in phase, pushing some cloud gas from the neutral into the ionized component (Section 3.2).

We assume solar metallicity ( $Z/Z_\odot = 1$ ) for the cloud, and  $Z/Z_\odot = 10^{-3}$  for the ambient gas. Miller & Bregman (2015) infer  $Z/Z_\odot = 0.3$  for the halo, and metallicities for the Smith Cloud and Complex C are estimated at  $Z/Z_\odot = 0.53^{+0.21}_{-0.15}$  (Fox et al. 2016) and  $Z/Z_\odot = 0.1\text{--}0.3$  (Collins et al. 2007), respectively. Therefore, our choices are not motivated by observations, but rather by an attempt (a) to clearly distinguish between cloud and halo material, and (b) to provide strict lower limits for cloud contamination estimates. Choosing metallicities closer to observed values would make it harder to distinguish between cloud and halo material, and higher halo metallicities would lead to faster cooling and thus more accretion of halo gas entrained in the cloud's wake. Taken together with the assumed halo temperature, our model cloud is therefore *less likely* to be contaminated than observed clouds. Even with these extreme choices, distinguishing between cloud and ambient material proves to be a challenge.

Cloud and halo gas are identified by passively advected scalar fields that can be imagined as a kind of dye being evolved together with the hydrodynamical equations (equations 2 and 3). The cloud mass at any time is given by

$$M_c = \int \rho(\mathbf{x}) C_c(\mathbf{x}) d^3x, \quad (7)$$

with a colour field  $C_c$  that is initialized to 1 within the cloud and 0 otherwise. The gas density is given by  $\rho = \mu m_H n$ , where we set  $\mu =$

1. Similarly, we identify original halo material, using a tracer field  $C_h$ .

Following Shin et al. (2008) and Goodson et al. (2017), we integrate the hydrodynamical equations within the rest frame of the cloud (Section A5) to improve the numerical accuracy. Since the cloud moves downward within the simulation box, the upper and lower boundary conditions in the vertical direction need to be modified. For the lower boundary condition, we calculate the hydrostatic density at the current vertical position of the boundary, and feed the corresponding hydrodynamic quantities to the boundary cells. The upper boundaries are set to 'open if leaving'.

## 2.2 Data analysis

Instead of post-processing, we have Athena generate position-position-velocity (PPV) cubes at 9 inclination angles from  $10^\circ$  to  $90^\circ$  on the fly (Section A1). The cubes contain H I-21 cm and optically thin generic metal absorption line spectra at each position. The metallicities can change drastically within the cloud. An average metallicity can be derived by adding up column densities along the line of sight. To get a more accurate measure of the metallicity at each position, we mimic the observational procedure to estimate column densities for individual velocity components for both H I-21 cm and the generic metal tracer. We decompose all spectra ( $\sim 6 \times 10^4$  spectra per time step, resulting in a total of  $\sim 4.5 \times 10^5$  spectra) into Gaussian components using ROHSA (Marchal et al. 2019, see Appendix B for details).

## 3 RESULTS

### 3.1 Raw data and overall evolution

The cloud passes through the stages typical for HVC simulations, from a flattened appearance (see Henley et al. 2017; Sander & Hensler 2021, for a demonstration) to an elongated head-tail structure. The cloud develops a diffuse, shock-compressed halo and a dense, small core. These are transients arising from the initial conditions, and they decay quickly to values consistent with the ambient pressure, leading to a more extended cloud that develops a tail (Fig. 1, top row). We skip those early stages in our analysis, since they are nearly completely determined by the choice of initial conditions (Cooper et al. 2009). Ram pressure decelerates the outer, more diffuse material, resulting in differential drag (Peek et al. 2007) and therefore in a centroid velocity gradient. The cloud begins to stretch out. Buoyancy effects in the stratified halo may start to play a role. At this point, a combination of radiative cooling and hydrodynamic instabilities fragments the cloud (Fig. 1, centre row). The cloud hits the Galactic plane at  $v_0 \sim 300 \text{ km s}^{-1}$ , close to the ballistic velocity, and in approximate agreement with the analytic estimates of Shull & Moss (2020). We discuss the amplitude of the impact velocity further in Section 4.1.4.

#### 3.1.1 Trajectories

Fig. 2 compares the model cloud trajectory with that of test particle clouds, following the approach of Benjamin & Danly (1997, see their fig. 3). We extend their discussion by considering mass accretion in addition to drag forces. The trajectories are calculated for three column densities ( $10^{18}, 10^{19}, 10^{20} \text{ cm}^{-2}$ ), including drag (label 'd') and both drag and mass accretion (label 'd + a'). Using  $d(mv)/dt = g(z) - C_d v^2 n_h(z) m/N_c$ , the underlying equations are

$$\dot{v} = g(z) - (C_d + C_a) v \dot{m}_l \quad (8)$$



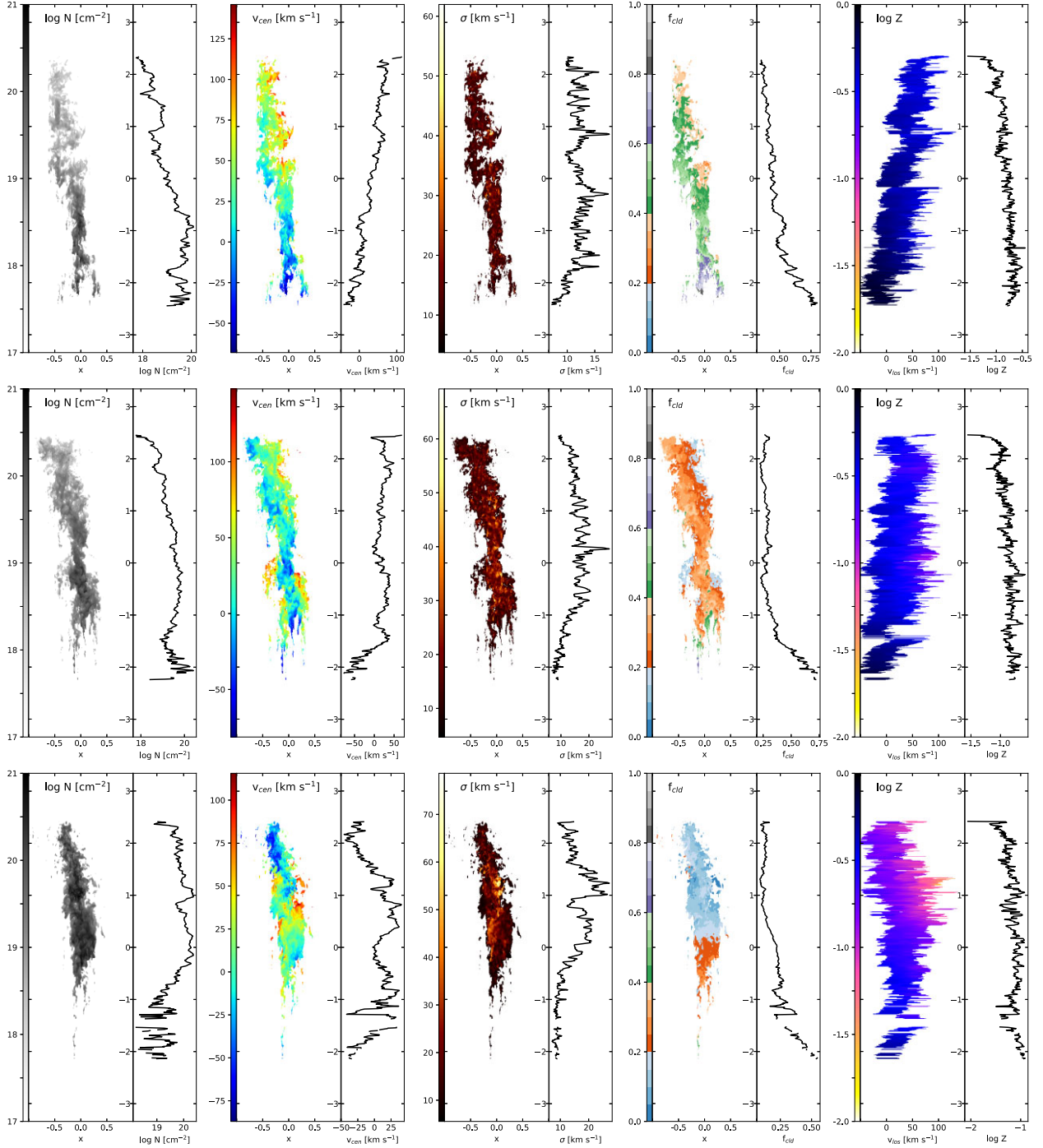


**Figure 1.** Integrated maps of the model cloud traveling through the halo toward the Galactic plane, at 200, 250, and 300 Myr (compare to Fig. 3). The cloud is viewed under an inclination angle of  $\alpha_i = 50^\circ$ . At  $\alpha_i = 90^\circ$  the cloud moves towards the observer. Each map is accompanied by its profile along the vertical axis. The spatial extent is given in kpc on the map's abscissa and the profile plot's ordinate. Colour bars show quantities indicated on the profile plot's abscissa. From left to right: Neutral (H I) column density, centroid velocity (equation [11]), total line width (equation [10]), cloud mass fraction, and metallicity in terms of centroid velocity and position along the cloud's long axis (see the text). The first three quantities are calculated from the ROHSA component fitting (Section B2) of H I-21 cm emission, and the last two quantities are based on the simulation raw data. At early times, column densities, centroid velocities, and metallicities show gradients, while at late times, the dynamics and hence the maps get more complex.

$$\dot{m}_l = \frac{n_h(z)}{N_c} |v|, \quad (9)$$

with  $\dot{z} \equiv v$ . For all models except the red dotted line of Shull & Moss (2020), the gravitational acceleration  $g(z) < 0$  is derived from the model halo (Section 2.1). The ambient halo density is given by  $n_h(z)$ ,  $C_d = 1$  is the drag coefficient,  $m_l \equiv \ln m(t)$  the logarithmic mass,

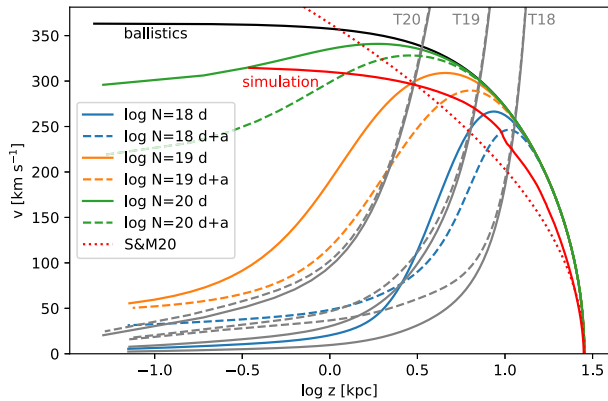


**Figure 2.** Phase space trajectories following Benjamin & Danly (1997) for ballistic clouds, compared to the hydrodynamical models (red curve). Blue, orange, and green trajectories stand for clouds at the indicated column densities. We compare models with drag only (solid lines), and with drag and accretion (dashed lines). Local terminal velocities (Benjamin & Danly 1997, their equation 2) are shown in grey for three column densities (labels T18, T19, T20). With increasing cloud column, drag is less efficient in decelerating the cloud. The red dotted line indicates the analytic estimate by Shull & Moss (2020) using a logarithmic potential.

and  $N_c(t)$  is the cloud’s column density. We quantify the accretion efficiency by an accretion coefficient,  $C_a = 1$ .

Drag and accretion result in the same expression, yet headed by different factors. Obviously, only accretion changes the mass. Low-column density clouds approach the terminal velocities (Benjamin & Danly 1997, shown in grey), and this is still valid for accreting clouds. The hydrodynamical cloud (red line) does not reach a local terminal velocity, but it approaches a ballistic trajectory. For the first 100 Myr, the cloud stays fairly coherent (Fig. 3b), dropping nearly ballistically through the halo. The cloud starts to fragment and to accrete material, breaking up the coherent structure. Meanwhile (Figs 1 and 3d), the column density is increasing, due to accretion of ambient material (Marinacci et al. 2010; Gritton et al. 2014; Fraternali et al. 2015; Gronke & Oh 2020) and because of the increasing ambient pressure (Heitsch & Putman 2009). For comparison, we also show the cloud velocity estimated by Shull & Moss (2020, red dotted line). This analytic estimate does not include drag, and therefore is expected to overpredict the velocity. In addition, Shull & Moss (2020) use a logarithmic potential, which is steeper closer to the disc than our composite potential (Section 2), but flatter at larger distances.

The cloud is sufficiently massive to punch through the disc, in contrast to the results from models comparing HVCs with and without dark matter halo confinement (Galyardt & Shelton 2016). The authors used a similar model setup and parameters as in Heitsch & Putman (2009) and this paper. The cloud is dropping through a stratified halo, eventually hitting the disc. The initial cloud mass is  $5 \times 10^6 M_\odot$ , and the cloud hits the disk at  $\sim 300 \text{ km s}^{-1}$ . Yet, Galyardt & Shelton (2016) find that their model cloud without dark matter confinement cannot punch through the disc. The difference seems to arise from the assumed Galactic disk densities. With  $n = 0.1 \text{ cm}^{-3}$ , our mid-plane density is on the order of the average cloud density. Yet, this mid-plane-density is somewhat low (Ferrière 2001; Cox 2005). Shull, Danforth & Anderson (2021) find  $n = n_{\text{HI}} + 2n_{\text{H}_2} = 0.5 \dots 1.5 \text{ cm}^{-3}$  at the solar circle. For their models, Galyardt & Shelton (2016) quote a mid-plane density of  $> 30 \text{ cm}^{-3}$  (their Fig. 2).

The simulation stops when cloud material reverses direction, since the role of the boundary conditions would have to be switched.

The motions are trans-sonic at this point for a considerable time. Transients interacting with the boundaries start to affect the cloud evolution and thus to invalidate the results.

### 3.1.2 Internal dynamics and peloton effect

Fig. 1 shows all quantities reconstructed from the ROHSA component fitting (Section B2) of H I-21 cm emission. The cloud is viewed under an inclination angle of  $\alpha_i = 60^\circ$ . At earlier times (top row), column densities, centroid velocities, metallicities, and cloud mass fractions exhibit gradients. After 50 Myr (centre row), the dynamics have turned more complicated and the distinct gradients (top row) have vanished. Of special interest is the structure of the centroid velocity, which starts developing inversions. Clumps of blue-shifted (faster) material appear over the whole length of the cloud. These inversions can also be seen in the associated vertical profiles. At early times, the fastest material is leading. Gas directly behind the cloud head is shielded from the ram pressure of the ambient medium (see also Forbes & Lin 2019). Radiative losses lead to condensation, so that the trailing gas contracts and – still shielded from ram pressure – can catch up to the leading head, eventually overtaking it. In other words, gas parcels within the cloud start to switch positions, not unlike in a peloton during bicycle races.

The line-of-sight velocity dispersion  $\sigma_{\text{los}}$  (the third column of Fig. 1) is generally smaller in the leading part of the cloud, indicating that these regions are less turbulent. This is consistent with some observations of HVCs (Brüns, Kerp & Pagels 2001; Peek et al. 2007), as are the gradients in the centroid velocity. At later times, the cloud starts to heat up dynamically and gets more turbulent. We calculate  $\sigma_{\text{los}}$  via the second moment of the position–position velocity cube,

$$\sigma_{\text{los}}^2 = \frac{\sum N(v_{\text{los}})(v_{\text{los}} - v_{\text{cen}})^2}{\sum N(v_{\text{los}})}, \quad (10)$$

where the sum extends over all velocity channels  $v_{\text{los}}$ ,  $N(v_{\text{los}})$  is the column density for a given velocity channel, and  $v_{\text{cen}}$  is the column-density-weighted centroid velocity

$$v_{\text{cen}} = \frac{\sum N(v_{\text{los}})v_{\text{los}}}{\sum N(v_{\text{los}})}. \quad (11)$$

Our calculation of  $\sigma_{\text{los}}$  contains both thermal and non-thermal contributions to the dispersion. However, at the evolutionary stage of the cloud, the bulk of the gas resides more or less uniformly in the warm regime, around  $T = 7 \times 10^3 \text{ K}$  (Fig. A1), corresponding to an isothermal sound speed of  $\approx 8 \text{ km s}^{-1}$ . This is smaller than most dispersions shown in the third column of Fig. 1, suggesting that gas dynamics, not gas temperatures, drive the variations in  $\sigma_{\text{los}}$ .

### 3.1.3 Metallicities and contamination

The fourth column of Fig. 1 shows the cloud mass fraction derived from the simulation data. The cloud mass fraction measures the amount of original cloud material in the observed (neutral) cloud. At early times, the cloud mass fraction indicates original cloud material contaminated by entrained gas along the cloud (grey to orange transition in the cloud mass fraction). With increasing time (center and bottom row), the cloud mass fraction drops, and the cloud consists largely of accreted material. The cloud mass fraction in the center row shows higher (green versus orange) values at the outskirts close to the leading head, corresponding to the red-shifted centroid velocities. This is again the peloton effect at work, with originally leading material (higher cloud mass fraction, green) being overtaken by newly accreted material (lower cloud mass fraction, orange).

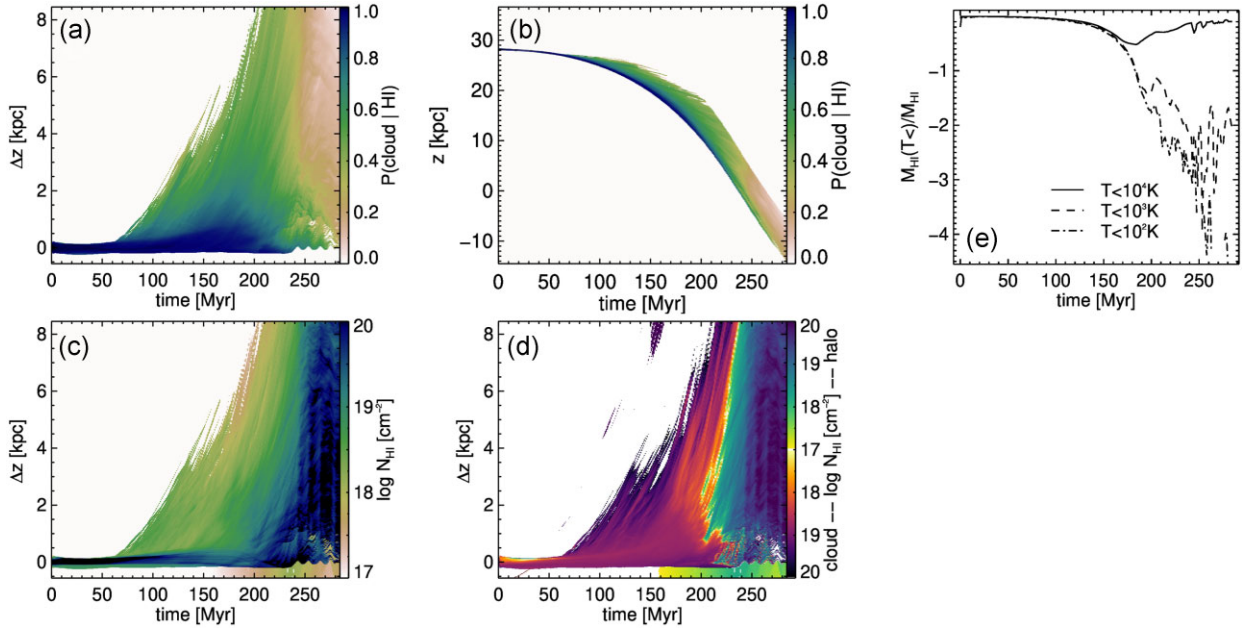


**Figure 3.** (a) Probability to detect original, neutral cloud gas (equation 12) as a function of position along the cloud’s major axis and model evolution time. The probability drops to less than 10 per cent at times  $>250$  Myr. (b) Same as (a), but along the cloud’s trajectory. (c) Average H I column density along the cloud’s long axis, similar to (a). The column density increases towards late times, indicating accretion. (d) H I column density split into contribution from original cloud (purple) and accreted halo (green/blue) material. (e) Mass history for H I at temperatures  $T < 10^4$  K,  $T < 10^3$  K and  $T < 10^2$  K, measuring the gas mass in the warm and cold neutral component. Subsequent analysis is limited to  $140 < t < 240$  Myr, after the cloud has lost the imprint of the initial conditions, and before it hits the Galactic plane.

The fifth column relates the channel velocity  $v_{\text{los}}$  at each position along the cloud’s long axis to the metallicity for each channel and position. We generate a position–velocity plot showing the metallicity of each position–velocity pair instead of the intensity. In other words, each position along the long axis of the cloud is represented by a spectrum where the brightness temperature has been replaced by the channel’s metallicity. This information is usually not accessible via observations unless high-resolution spectra are available for both tracers, but it provides us with a detailed view of the correlation between line-of-sight velocity and metallicity. The abscissa shows the channel velocity over the same range as indicated by the colourbar in the centroid velocity maps (second column). The ordinate shows, as in all other panels, the position along the cloud’s long axis. Colour indicates the metallicity for each position and velocity channel. The position–velocity map is derived from the full position–position–velocity cube by integrating over the  $x$  (horizontal) axis. At early times (top row), the position–velocity distribution shows a gradient from blue-shifted, leading velocities, to red-shifted, trailing ones. The gradient indicates that the ‘tail’ of the cloud is red-shifted with respect to the head, and therefore lagging behind the head. In the bottom panel, this gradient has vanished, but *metallicities* are generally lower at higher velocity for all positions, suggesting contamination. Ambient material at low metallicity is entrained all along the cloud, but it lags behind the main body of the cloud, and therefore travels at more positive (red-shifted) line-of-sight velocities.

Since most of the cloud material gets replaced by ambient gas, the earlier statement about heating of cloud material should not be taken literally. The velocity dispersion increases mostly because ambient material is entrained in the cloud’s wake, then cools and later appears as neutral gas (Gronke & Oh 2020). Actual heating of original cloud material plays only a minor role. While the cloud appears to be

heated dynamically, this is just an effect of coherently moving cloud material being replaced by more turbulent ambient material.

### 3.2 Probability for cloud material

The probability for neutral gas to be cloud material  $P(\text{cloud}|\text{H I})$  allows us to assess whether metallicities can constrain cloud origin scenarios. If  $z$  is the coordinate along the cloud’s long axis, also taken as the local tangent to the trajectory, the probabilities are calculated by determining the ratio of the tracer fields in terms of a mixing parameter averaged laterally over all positions at a fixed  $z$ ,

$$P(\text{cloud}|\text{H I}, z) = \frac{1}{2} \left( 1 + \frac{\bar{C}_c(z) - \bar{C}_h(z)}{\bar{C}_c(z) + \bar{C}_h(z)} \right), \quad (12)$$

where the subscript  $c, h$  denote cloud and halo material, respectively. The average colour field  $\bar{C}_c(z)$  is defined as

$$\bar{C}_c(z) = \frac{\int \rho(\mathbf{x}) C_c(\mathbf{x}) (1 - x_i(\mathbf{x})) d\mathbf{x} d\mathbf{y}}{\int \rho(\mathbf{x}) (1 - x_i(\mathbf{x})) d\mathbf{x} d\mathbf{y}}, \quad (13)$$

where  $x$  and  $y$  are the lateral axes, i.e. perpendicular to the trajectory. The local gas density is given by  $\rho$ , and the ionization fraction is  $x_i(\mathbf{x})$ . The probability  $P(\text{cloud}|\text{H I}, z)$  is normalized to 1 for each  $z$ .

Fig. 3 summarizes the time evolution of the probability to find cloud material along the long axis of the cloud (panels [a,b]). Initially, the neutral gas component (panel [c,d]) consists of 100 per cent cloud material, but the probabilities decrease once a tail forms around 100 Myr. The cloud ends up mostly consisting of accreted material. Probabilities  $<1$  indicate that ambient material transitioned to the neutral phase via cooling (compare panels a, c, d). Its spread along the trajectory (panel b) suggests that this material is entrained in the wake of the cloud, consistent with the metallicity and cloud mass fraction maps of Fig. 1. Fig. 3(e) shows the mass of gas at temperatures  $\leq 10^4$ ,



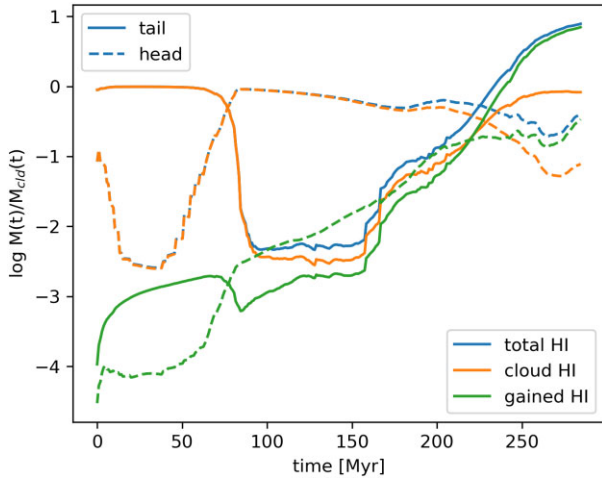


**Figure 4.** Time evolution of mass fractions over the whole cloud extent (solid) and the leading third (head) of the cloud. Mass fractions refer to the current cloud mass. The cloud tail accretes a factor of  $\sim 30$  more material than the head. The cloud ends up with  $\sim 10$  percent of original cloud material, both in head and tail.

$10^3$ ,  $10^2$  K, as a measure of the cold gas component. At the end of the burn-in phase, the cold neutral component drops to less than a per cent of the neutral cloud mass because of the initial overpressure within the cloud (Section 2.1). Once the cloud hits the plane at  $t \sim 240$  Myr, the neutral component grows again, via accretion.

Fig. 4 provides a simplified view of the distribution of accreted mass. We split the cloud into a lower third (the ‘head’ – dashed lines) and the remaining two thirds (the ‘tail’ – solid lines). The inversion between head and tail in the total H I gas indicates that initially, the head is heated by compression (dip in mass fraction around 20 Myr) and then starts to cool again. Meanwhile, the tail loses most of its neutral gas. At around 100 Myr, the total H I mass (blue) rises above the cloud H I mass (orange), a trend that is amplified until the end, when  $\sim 90$  percent of the tail’s neutral gas consist of accreted gas. Gained H I (green) supports this interpretation, since it converges on the total H I mass. The mass fraction for the head show a similar evolution, except that they stay a factor of  $\sim 30$  below the tail mass fractions at late times. Therefore, most of the gas is accreted in the tail, consistent with Henley et al. (2017). The mass ratios demonstrate that for our evolved cloud, only 10 percent of the neutral gas is original cloud material. See also Sections 3.4 and 4.2.

We restrict the subsequent analysis to the time range between 140 and 240 Myr, when the cloud has evolved away from its initial conditions, but has not yet crossed the disc’s mid-plane.

### 3.3 Thermal evolution

The neutral gas mass drops again after the cloud punches through the disc (Fig. 3e), suggesting that the ambient thermal pressure may be the driver for the overall mass evolution. Fig. 5 takes a closer look at the thermal state of all gas in the simulation domain. Pressure (Fig. 5a), temperature (5b) and density (5c) distributions in terms of mass fractions are shown against simulation time. Red lines indicate ambient halo values for pressure and density. The bulk of the ambient gas stays at the isothermal halo temperature of  $2.2 \times 10^6$  K, because of the long cooling time. Grey lines in the temperature (Fig. 5b) and density (Fig. 5c) history show the thermal equilibrium value derived from the cooling curve (Fig. A1) at the current ambient pressure. At the higher pressures around vertical distances of  $z = 0$  (Galactic

plane), two equilibrium solutions are possible, one for warm (solid) and one for cold gas (dashed). The red and grey lines stand for reference values taken at the cloud’s centre of mass.

The pressure distribution (Fig. 5a) is constrained by the ambient gas pressure for the most part. Ram pressure drives the cloud gas above the red line, and cloud gas in the wake will be at lower pressure (blue regions below the red line). Approaching the plane, the pressure increases overall. Once the cloud punches through the disk, the ambient pressure begins to drop, and the leading (faster) cloud gas (thin blue line below the red line beyond 240 Myr) drops more rapidly than the reference value at the centre of mass.

The dense, cold cloud gas of the initial conditions is nearly gone at the end of the burn-in phase (around 140 Myr), leaving only warm gas at  $T \sim 10^4$  K. Since the temperatures in the three thermal regimes (hot, warm, cold) are mostly constant, the densities (Fig. 5c) follow a shape similar to the pressure (Fig. 5a). At around 100 Myr, mass starts to flow from the hot component at  $T = 2.2 \times 10^6$  K to the warm gas. Once the cloud approaches the plane, the pressure increases such that density and temperature can access the two thermal equilibrium solutions. The warm phase ( $\sim 10^4$  K) tries to transit to the cold phase, but dynamics prevent a full conversion, so that it reaches only the unstable neutral phase (Murray et al. 2018). The onset of the transition can be seen around 150 Myr and 200 Myr (Fig. 5b), with gas moving from  $T = 10^4$  K to lower temperatures. While the pressure at  $P/k_B > 3 \times 10^3$  K  $\text{cm}^{-3}$  should suffice for warm and cold neutral gas to co-exist at the same pressure (compare to Fig. A1), dynamical heating competes with radiative cooling (Gazol et al. 2001, though in a different context), suppressing the full formation of a cold phase.

Most of the cloud’s thermal state and thus the presence of neutral gas is determined by the ambient pressure (Wolfire et al. 1995b), while dynamical effects lead to a gradual transition between the stable phases. Yet, conversion from warm to cold neutral medium is not complete by any means, rather, any gas leaving the warm neutral phase cools down only to the unstable neutral phase.

### 3.4 Time evolution and inclination angle

Fig. 6 shows the time evolution between 140 and 240 Myr (see Fig. 3) of the cloud profiles in dependence of inclination angles, from  $\alpha_i = 10^\circ$  (nearly in the plane of sky) to  $\alpha_i = 90^\circ$  (cloud moving towards observer). Quantities and colour schemes are identical to those used in Fig. 1.

The cloud stretches out and develops a head–tail structure, which then breaks up into fragments moving at different speeds as indicated by the blue-shifted material throughout the cloud for larger  $\alpha_i$  (centroid velocities, second column). Metallicities and cloud mass fractions drop with time, indicating contamination of the cloud by ambient material. Original cloud material is indicated by grey tones (cloud mass fraction, fifth column), while ambient gas is shown in blue tones. At a given time, the cloud mass fraction decreases from head (bottom) to tail (top) for all angles but  $90^\circ$ . Therefore, the tail is contaminated faster than the head, suggesting contamination via accretion into the cloud wake rather than by sweep-up of material by the head. Despite the peloton effect and accretion, finding original cloud material near the leading part of the cloud is more likely than towards the trailing part, consistent with the results of Henley et al. (2017). The cloud is predominantly contaminated by entraining ambient material in its wake, and not via sweepup and compression. If sweepup and compression of ambient material were the main accretion mechanism, the leading part of the cloud should contain relatively *less* original cloud material than the trailing part. Gritton et al. (2017) point out that for supersonic motions, condensation



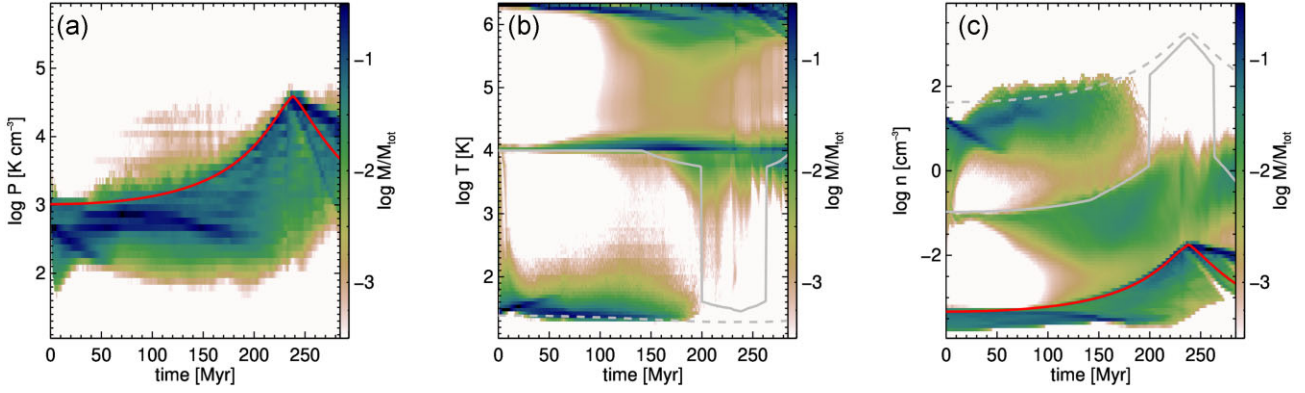


**Figure 5.** Pressure (a), temperature (b), and density (c) mass fraction distribution against time in the simulation domain. All gas is shown. The ambient halo pressure at the cloud’s centre of mass (reference position) is shown as a red line in (a), and the corresponding halo density as a red line in (c). The halo temperature is constant at  $T = 2.2 \times 10^6$  K. The grey curves show the thermal equilibrium temperature (b) and density (c) for the dense cloud gas (dashed), and for the cloud envelope (solid). At higher pressures, there are two solutions, indicating a thermally bi-stable gas (Fig. A1). The ambient pressure drop co-incides with the drop in neutral cloud mass (Fig. 3d).

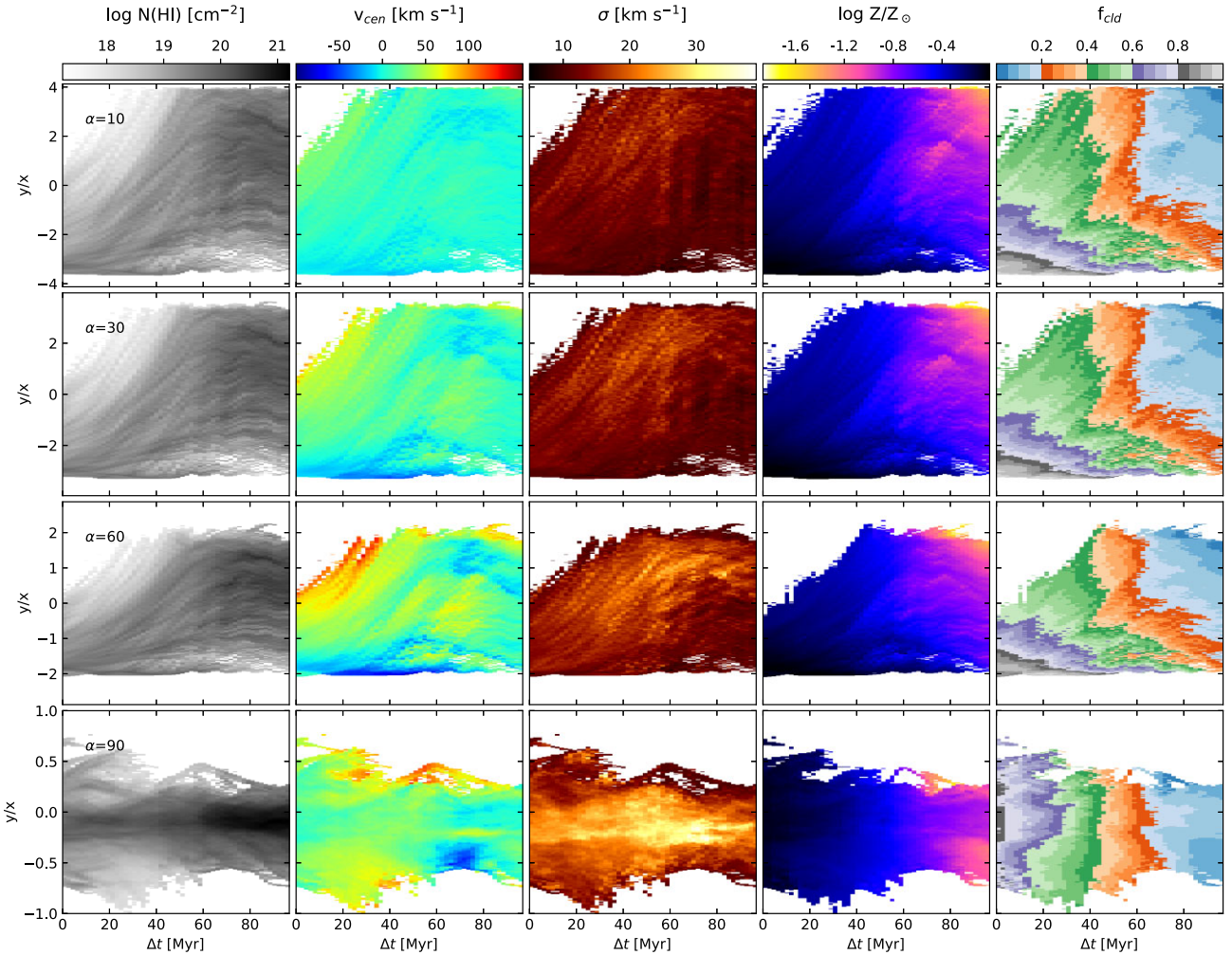


**Figure 6.** Laterally averaged profiles along the cloud’s long axis, against time after burn-in (140 Myr), for four inclination angles. Quantities shown and colour schemes are identical to those in Fig. 1. The ordinate shows the position along the cloud’s long axis, in units of the simulation domain’s lateral extent. From left to right: Column density, centroid velocity, non-thermal line-width, metallicity, and cloud mass fraction. Grey tones in the cloud mass fraction indicate highest fraction of original material. Therefore, material is accreted predominantly in the tail (top), and not in the head (bottom) of the cloud. All inclination angles except  $\alpha_i = 90^\circ$  (head-on) show a gradient in metallicity and cloud mass fraction.

at the head of the cloud can be suppressed because a bow shock develops, but that material still can condense in the wake. At  $\sim 300 \text{ km s}^{-1}$  (Fig. 2), the cloud travels supersonically with respect to the background medium.

Histograms of characteristic cloud measures (Fig. 7) highlight how accretion affects the overall cloud properties. The average column density increases with time, while the average metallicity and cloud mass fraction drop by more than a factor of 10. The width of both metallicity and cloud mass fraction distributions decrease with time for larger inclination angles. The cloud accretes ambient material, replacing the original cloud material, and thus resulting in a more homogeneous composition. For  $\alpha = 10^\circ$ , the metallicity distribution develops a tail toward lower values, resulting in a spread of over 1.5 dex. For small inclination angles, more material at low column densities contributes to the lines of sight. Since low column densities are more likely to arise from accreted material (Section 3.6, for our model parameters) lower metallicities indicating ambient gas.

The cloud decelerates once it has punched through the disc. This reduces the drag along the cloud, and thus the velocity differences of accreted material between different cloud locations. Therefore, the overall velocity dispersion drops, and the cloud becomes dynamically more coherent.

Only extreme inclination angles ( $\alpha_i = 10^\circ, 90^\circ$ ) affect the overall appearance of the cloud (Fig. 6). For small inclination angles, relative velocities along the cloud trajectory are suppressed, and therefore, the peloton effect cannot be observed. Metallicity estimates and distributions are consistent except for fully head-on trajectories ( $\alpha_i = 90^\circ$ ). Because of the large aspect ratio of cloud length over width, only  $\alpha_i \approx 90^\circ$  leads to confusion in metallicities. Variations in metallicities and cloud mass fraction along the cloud's long axis are consistent except for  $\alpha_i \approx 90^\circ$ .

The probability to find original cloud material decreases from head to tail (Fig. 6, last column showing the cloud mass fraction), and it strongly depends on position, time, and inclination angle. Note that finding original cloud material is related, but not identical to finding sight-lines with high original cloud material content. The difference can be seen by comparing the cloud mass fractions in Figs 1 and 6. Small pockets of sight-lines with  $\sim 50$  per cent cloud material survive, yet their area coverage is vanishingly small compared to the cloud area (see also Section 3.6).

Distributions (Fig. 7) are differently affected by inclination angles. Column densities generally increase for higher  $\alpha_i$ , but their distribution narrows, while the centroid velocities show the reverse effect, since for low  $\alpha_i$ , the lag of cloud material along the trajectory does not contribute to the velocity spread. At larger inclination angles, at least two centroid velocity components are discernible. Linewidths also increase with increasing  $\alpha_i$ , as more gas is mixed along the line of sight, leading to velocity crowding. Metallicities and cloud mass fraction distributions are mostly unaffected by the viewing angle, suggesting that the latter two – especially metallicities in terms of observables – are robust against variation in  $\alpha_i$ .

### 3.5 Velocity lags and metallicity

Our discussion suggests that lower cloud mass fractions and ambient (in our case, lower) metallicities should be correlated with larger velocity lags along the cloud. Fig. 8 confirms this expectation for early times. The 2D histograms of cloud mass fraction (top) against centroid velocity display a distinct negative gradient from small ( $v_{\text{cen}} = 0$ ) to large lags ( $v_{\text{cen}} > 0$ ). Metallicities (bottom) mostly follow the same trend. The correlation becomes more pronounced for larger  $\alpha_i$ , since turbulent lateral motions of the cloud material do not

contribute. At late times, both cloud mass fractions and metallicities develop two distinct peaks, both spread out over similar velocity ranges. This is a dynamic signature of the peloton effect: original and ambient material are mixed throughout the cloud, travelling at similar velocities.

### 3.6 Column densities and metallicities

Due to its proximity, the HVC complex with probably the highest number of abundance measurements is Complex C (Wakker et al. 1999b; Richter et al. 2001; Tripp et al. 2003; Collins, Shull & Giroux 2003; Collins et al. 2007; Shull et al. 2011). Collins et al. (2007) explore correlations between [O/H] abundances and H I column densities as a signature of mixing with ambient gas, hypothesizing that higher column densities should show less contamination with ambient material. While present, the observed trend is weak due to measurement uncertainties. The fourth column of Fig. 1 provides a modeler's version of fig. 8 of Collins et al. (2007). In the center row, the cloud mass fraction at the cloud edge (around  $y = 0$ ) is lower than that of the cloud's main body. These regions coincide with lower column densities (first column). Note that while Collins et al. (2007) would expect an anticorrelation between metallicity and column density, for our model parameters a positive correlation between column density and metallicity indicates mixing between ambient and cloud gas.

Fig. 9 provides a more detailed view, showing the joint distributions of cloud mass fraction as a proxy for metallicity, and column density. We show the cloud mass fraction, since the metallicities are model-dependent. A positive correlation between cloud mass fraction and column density indicates mixing and accretion. Indeed, for the first two time instances (top and center row), all viewing angles suggest a positive trend. When the cloud is about to punch through the disk, column densities rapidly increase, and a substantial amount of ambient material is accreted. This leads to a flat distribution with cloud mass fraction – most of the neutral gas is now stemming from the ambient medium.

The specific choice of cloud and halo metallicities in our model precludes quantitative predictions of metallicities within any given cloud. Yet, the metallicity gradient (Fig. 6) across a cloud provides an opportunity to distinguish between enrichment or dilution of cloud material, which will occur when the cloud's metallicity is lower or higher than that of the ambient gas, respectively. In the case of enrichment, the metallicity gradient along the cloud should be positive, since material of higher metallicity gets successively entrained in the cloud's wake (Fig. 4). In the case of dilution (as in our model cloud), the metallicity gradient should be negative, as low-metallicity gas gets entrained. While specific values will depend on several factors including the metallicity contrast between the cloud and the ambient gas, estimating the metallicity gradient across a given cloud even by two or three sightlines may provide information about the relative metallicities.

The Smith Cloud can serve as an example. Although three metallicity measurements for the Smith Cloud (Fox et al. 2016) do not show a clear gradient, the two sight-lines close to the head of the cloud show higher values ( $[S/H] = -0.09 \pm 0.33$  and  $-0.14 \pm 0.13$ ), while the cloud tail has a lower value of  $[S/H] = -0.58 \pm 0.20$ . If we group the first two values together, the above reasoning would lead us to conclude that the Smith Cloud's material has been diluted (not enriched) by ambient gas of lower metallicity. On the other hand, Henley et al. (2017) focus on the two higher metallicity estimates and conclude that their models are consistent with the Smith Cloud having been enriched over time by high-metallicity ambient gas, but

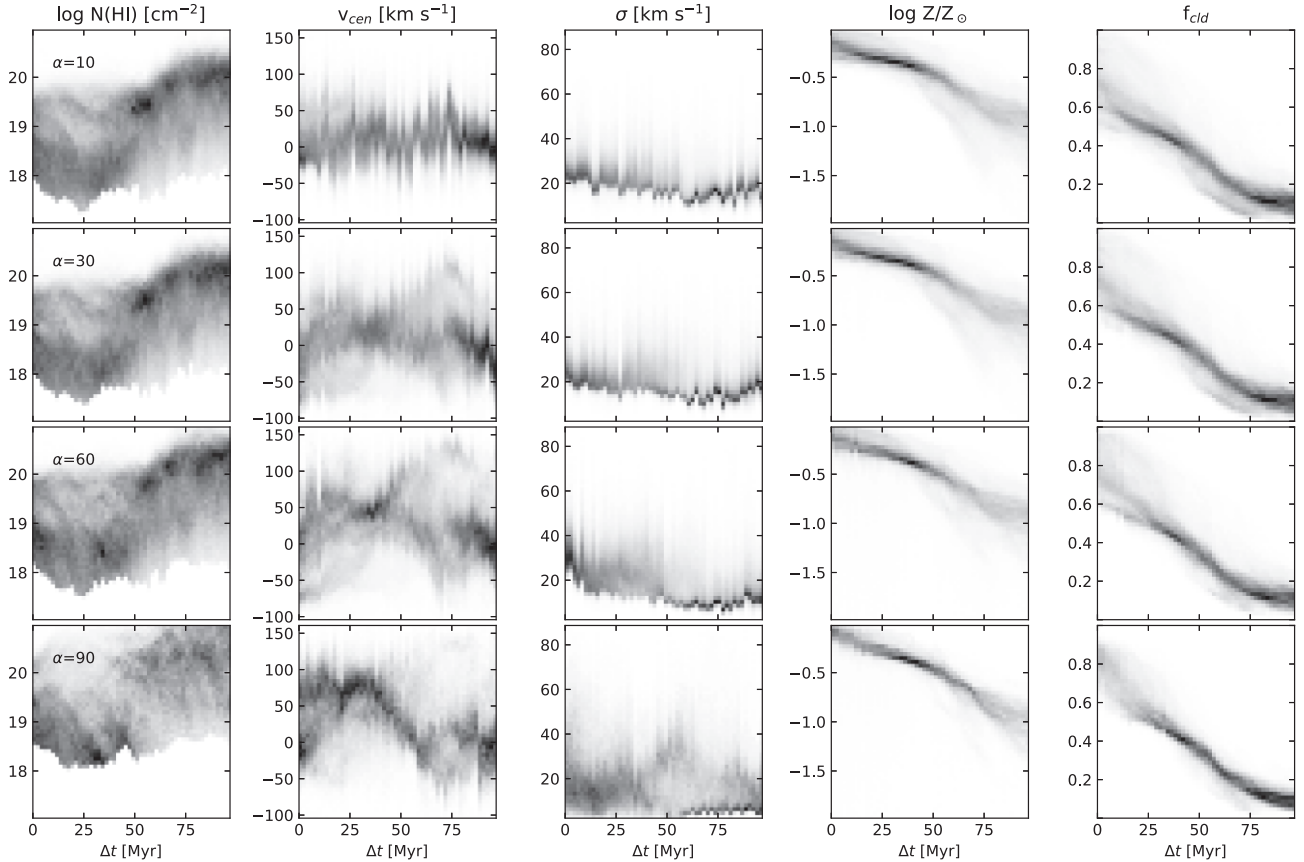


**Figure 7.** Histograms of all quantities shown in Fig. 6, against time after burn-in (140 Myr), for all inclination angles. From left to right: Column density, centroid velocity, non-thermal line-width, metallicity, and cloud mass fraction.

this does not explain the lower metallicity measured in the cloud wake. More observational metallicity constraints, in both the cool clouds and the hot ambient gas, are needed for further progress.

Fig. 9 provides a measure for the probability to find sight-lines with high original cloud material content, at a given point in the cloud’s evolution. While the overall cloud mass fraction drops with time, pockets of sight-lines with a high cloud mass fraction survive (centre row, lower inclination angles). Yet their area coverage is small compared to that of accreted material. For example, the probability to find sight-lines with  $f_{\text{cl}} > 0.5$  at  $\Delta t = 80$  Myr is less than 1 per cent.

## 4 DISCUSSION

We presented an analysis of a hydrodynamical simulation of a gas cloud traveling through the Galactic halo, determining the probability to find original cloud material within the observed cloud at any given time and viewing angle. The model assumes cloud formation via infall, possibly due to stripping from dwarf satellites. Other origin scenarios for cloud formation have been discussed elsewhere (e.g. Ji, Oh & McCourt 2018, for *in situ* formation).

### 4.1 Caveats

#### 4.1.1 Missing physics

We leave out the effects of thermal conduction and magnetic fields. Brüggén & Scannapieco (2016) investigated the role of heat conduction with 3D adaptive mesh refinement models, concluding

that electron thermal conduction does play a role in the evaporation of clouds of low column densities. Though applied to a different scenario, namely the acceleration of cold clouds in a galactic wind, the underlying physics is similar. Two-dimensional models of cloud disruption including radiative cooling and heat conduction (Vieser & Hensler 2007a, b; Armillotta et al. 2017) have shown that heat conduction can help to stabilize the cloud against disruption. The latter authors exploit the advantages of reduced dimensions and explore a range of cloud radii and masses. Kooij, Grønnow & Fraternali (2021) demonstrate numerically that magnetic fields might suppress thermal conduction (Spitzer 1962) and thus help cool gas ‘survive’. Yet they point out that thermal conduction – even if suppressed – still affects the evolution of a cloud.

In a similar study of cloud acceleration in hot winds, McCourt et al. (2015) conclude that, when using tangled magnetic fields, the clouds start to move with the background medium in near pressure equilibrium, rather than being disrupted. The magnetic field suppresses the dynamical instabilities (see also Grønnow et al. 2017), while it links the cloud to the ambient gas via sweep-up of field lines, thus increasing the drag force above hydrodynamic values. To capture the effect of magnetic fields fully, three-dimensional simulations are necessary (Grønnow, Tepper-García & Bland-Hawthorn 2018), since in two dimensions, interchange modes cannot develop (Stone & Gardiner 2007). Still, magnetic fields seem capable of suppressing some of the condensation of ambient material into the wake (Grønnow et al. 2018, see also Field 1965 for the suppression of thermal instability in the presence of magnetic fields); therefore, we expect that including magnetic fields in our models would slow



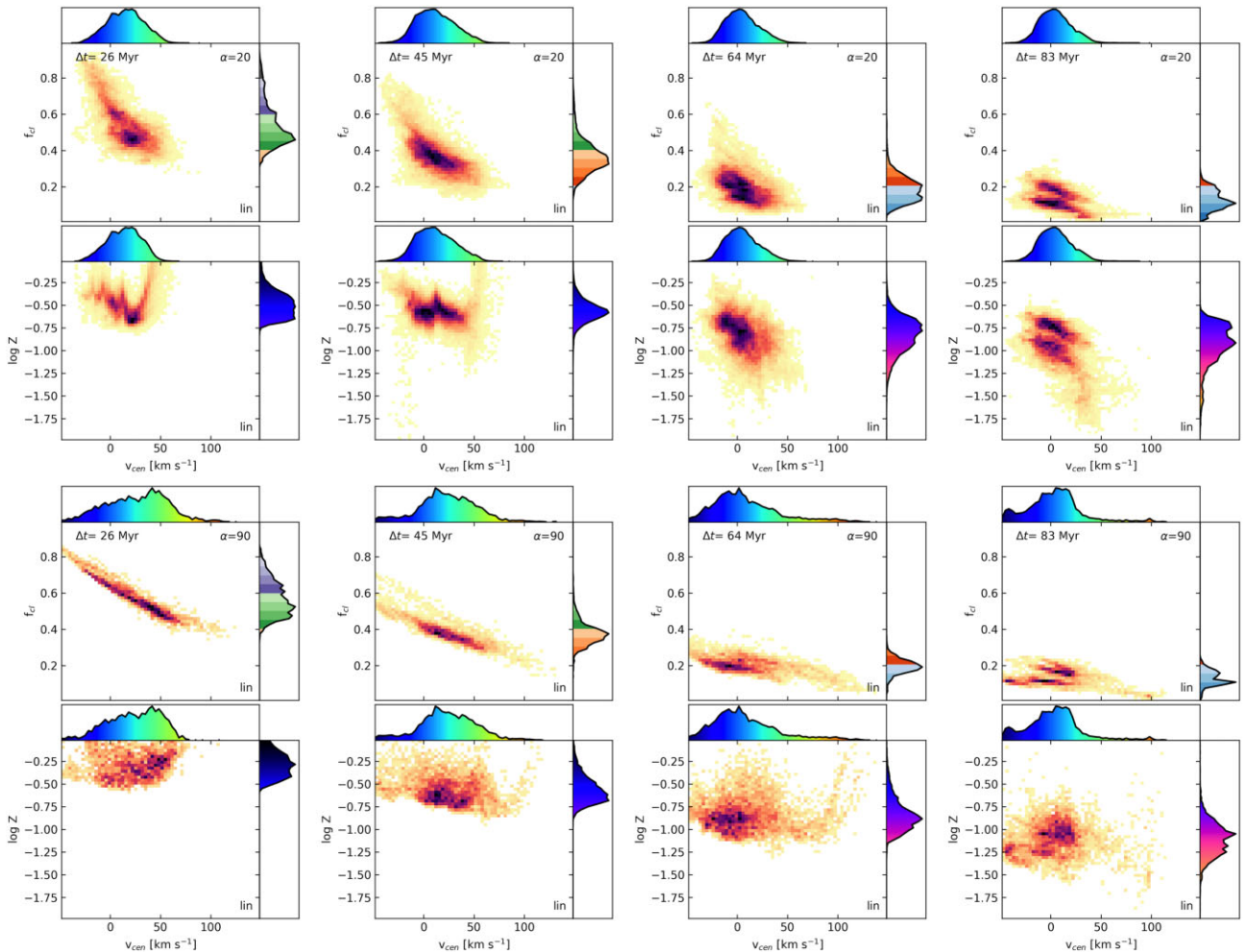


**Figure 8.** Time history (columns) of the cloud mass fraction  $f_c$  (top) and metallicity  $\log Z$  (bottom) as function of the centroid velocity ( $x$ -axis), for several inclination angles (rows). Times  $\Delta t$  are given after burn-in (140 Myr). Cloud mass fractions systematically drop with higher (red-shifted) velocities, and with increasing time. For the metallicities, both statements are generally true, though the viewing angles can hide the signature. Colour scales of marginalized histograms are identical to those of Fig. 1.

down the cloud and suppress cloud disruption, resulting in less mass lost and therefore in a higher probability to detect cloud material along the tail (Fig. 3).

#### 4.1.2 Metallicities and disk structure

Our choice of initial cloud and specifically halo metallicities will reduce the condensation of halo gas in the wake of the cloud compared to more realistic (higher) halo metallicities. Therefore, our contamination estimates are *lower* limits, since higher halo metallicities would lead to more gas condensing in the wake of the cloud via cooling. Also, metallicity gradients would be less steep than found in our analysis. Omitting the thin disc with its colder and denser (neutral) gas component in our simplified halo model also suppresses accretion of ambient gas.

#### 4.1.3 Beam smearing

We assume pencil beams for both absorption and emission. All HVC metallicity estimates are derived by combining H I 21 cm measurements taken at a finite beamwidth with UV metal-line

measurements taken at an infinitesimal beam (pencil) width and are therefore sensitive to beam-smearing effects, in which small-scale (sub-beam) structure in the radio data could impact the actual H I column along the UV pencil beam. Wakker et al. (1999a), Wakker et al. (2001) quantified this effect for a few lines of sight, extending to a list of H I 21 cm columns for all available HVC sightlines (Wakker, Lockman & Brown 2011). They estimated that, typically, H I columns are accurate within 10–25 per cent, or  $\pm 0.04$ –0.10 in  $\log N_H$ . We will leave the consideration of beam-smearing effects for a future contribution.

#### 4.1.4 Impact velocity

The cloud’s velocity relative to the ambient gas is not only relevant for hydrodynamical considerations, since instabilities can be suppressed for supersonic motions (Chandrasekhar 1961) and therefore the accretion mechanism changes (Gritton et al. 2017), but it also could serve as a check against observations. Yet, three-dimensional velocity information for HVCs is available only in rare circumstances.

Lockman et al. (2008) determined the three spatial velocity components of the Smith Cloud, with a total space velocity of  $V_{\text{tot}} = 300 \text{ km s}^{-1}$  and a vertical component of  $73 \pm 26 \text{ km s}^{-1}$



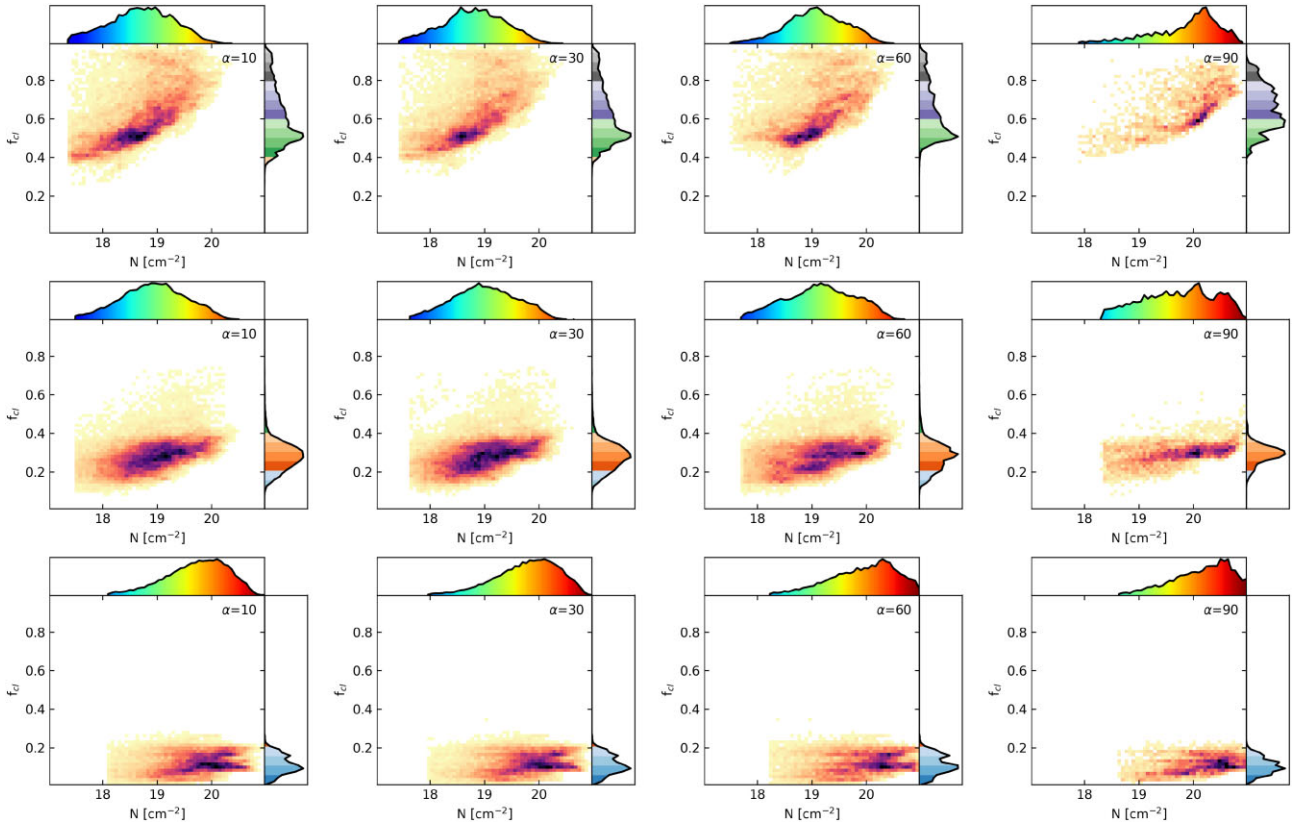


**Figure 9.** 2D histograms of cloud mass fraction against column density, to test for correlation between metallicity and column density. A positive correlation indicates mixing between cloud and ambient gas. Colours stand for the number of sightlines. Times are  $\Delta t = 60, 80, 100$  Myr (top to bottom). Different viewing angles are arranged horizontally, from in-the-plane (left) to a head-on view (right).

at which the cloud is approaching the disc. Its orbit is highly inclined and prograde, so that the Smith Cloud’s velocity relative to the ambient gas would expected to be much less than  $V_{\text{tot}}$ . Heitsch et al. (2016) proposed a method to reconstruct the three-dimensional cloud propagation direction required to calculate  $V_{\text{tot}}$ , based on the cloud morphology in the position-velocity plane and  $v_{\text{LSR}}$ . Applying the method to a subset of clouds identified in HIPASS (Putman et al. 2002), they estimate  $V_{\text{tot}}$  of up to  $>300 \text{ km s}^{-1}$  for a few clouds. Yet, these estimates, and the resulting relative speed with respect to the ambient gas, strongly depend on the assumed halo gas rotation model.

Theoretical estimates of the infall velocity depend on the cloud’s starting point, on the gravitational potential, and on whether drag is included. Shull & Moss (2020) find infall velocities of  $\sim 350 \text{ km s}^{-1}$  without drag and a logarithmic potential (Fig. 2), while Benjamin & Danly (1997) including drag estimate terminal velocities of  $\sim 150 \text{ km s}^{-1}$ . Self-consistent models in which the cloud is dropped in a stratified halo (Heitsch & Putman 2009; Sander & Hensler 2021) reach cloud velocities between 150 and  $>300 \text{ km s}^{-1}$ . Wind-tunnel experiments explore ranges of  $100\text{--}350 \text{ km s}^{-1}$  (e.g. Kwak, Henley & Shelton 2011).

#### 4.2 Consequences for observations

(i) The peloton effect (Section 3.1.2) could be detected in three ways: (a) High-resolution (interferometry) observations at the leading head of a cloud would exhibit ‘unordered’ velocity fields not following a systematic velocity gradient from head to tail (Fig. 6).

(b) The (thermally) cooler head would show a large non-thermal component. This could be looked for in HI 21 cm data as well as in UV absorption lines (Fig. 6). (c) Joint distributions of metallicity and centroid velocities would show double or multiple peaks (Fig. 8).

(ii) Using metallicities as diagnostics for cloud origin is complicated mostly by substantial contamination especially of the trailing cloud parts due to accretion of ambient gas (Figs 3, 4, 6, see also Henley et al. 2017). Though the leading cloud part is less prone to accrete material specifically at supersonic motions, the peloton effect will eventually also lead to contamination, flattening the metallicity gradient to a point where distinguishing between original and accreted gas might be impossible.

(iii) Not only does the mass fraction of original cloud material drop with time, but also the area coverage of sight-lines with high original cloud mass fraction decreases rapidly. The probability to find such sight-lines strongly depends on inclination angle and time (Figs 1 and 6). Fig. 9 suggests that the probability to find sight-lines with  $f_{\text{cl}} > 0.5$  is vanishingly small for evolved clouds. Therefore, in all likelihood, metallicity measurements in HVCs will not represent original cloud properties, but metallicity gradients will provide insight about cloud contamination.

(iv) While the H I column densities vary over nearly two orders of magnitude at any time, the metallicities are spread over half a dex at most at any given time (Fig. 7). Metallicities drop with time due to accretion well beyond observational uncertainties (Fox et al. 2016), yet an individual snapshot shows a largely uniform metallicity. The spread is larger than observational uncertainties at any given time, allowing observational distinction between cloud and ambient

material only *if their metallicities differ sufficiently*. Viewing angles do not affect the metallicity estimates.

(v) If the ambient metallicity is known, variations of the metallicity along the cloud can provide information about whether gas has been mostly accreted via compression at the leading head or via condensation in the trailing tail.

(vi) Metallicity gradients along the cloud trajectory can provide insight about the relative metallicities of cloud and ambient gas, based on the observation that ambient material is successively entrained in the cloud's wake (Fig. 6, Section 3.6).

(vii) Correlations between metallicity and column density can indicate the presence of cloud gas mixing with ambient gas (Collins et al. 2007). Fig. 9 suggests that such a correlation would strongly depend on the evolutionary state of the cloud – if such a concept is applicable at all. A ‘pristine’ cloud traveling through the halo would show a correlation between metallicity and column density, but once the majority of a cloud's mass is actually coming from the ambient gas, the correlation between metallicity and column density should be flat.

### 4.3 Outlook

While our parameter choices do allow us to set strong lower limits on contamination, ultimately, exploring a range of halo and cloud metallicities, cloud masses, and trajectories might seem advisable to further constrain how accretion affects realistic clouds. Yet, based on our parameter choices, we do not expect results to change qualitatively.

Our model addresses the evolution and contamination of an infalling cloud, but similar contamination mechanisms might be expected for outflowing clouds driven by Galactic winds (e.g. Di Teodoro et al. 2018; Lockman, Di Teodoro & McClure-Griffiths 2020). Depending on the balance between ram pressure acceleration by the wind and gravitational acceleration, outflow models might be closer to wind-tunnel experiments than envisaged here.

## 5 CONCLUSIONS

We use hydrodynamic simulations of infalling high-velocity clouds run with a modified version of Athena (Stone et al. 2008) to probe how reliably metallicity measurements can identify ‘original’ cloud material over time, along the cloud, and under a range of viewing angles. The model parameters are chosen to provide conservative (strong) limits on cloud contamination by ambient material. Our analysis has led us to conclude the following:

(i) The cloud is contaminated nearly linearly with time, until most of the original cloud material has been replaced by accreted gas (Fig. 7). The cloud is well defined at any *fixed* time, but not *across* time, and thus is not defined by constancy in its constituent gas particles, but by self-propagating density and pressure perturbations. The energy necessary to reform the cloud is provided by the potential energy of the overdensities.

(ii) Our super-sonically moving cloud is to some extent contaminated at its leading edge by sweep-up, but mostly along the cloud tail, due to thermal condensation into the wake of the cloud (Fig. 6). The thermal state of cloud gas – whether original or accreted – is largely controlled by the ambient pressure (Fig. 5) and the cloud dynamics.

(iii) The cloud dynamics can get extremely complex, with initially lagging material that is shielded from ram pressure catching up to the head, and even passing the head, of the cloud (peloton effect). This would affect centroid velocity gradients and thus drag estimates

(Peek et al. 2007), and it could also introduce uncertainties in metallicity gradients.

(iv) While the dynamical quantities (centroid velocity and velocity dispersion) depend on the inclination angle, the overall metallicities are unaffected by inclination within observational uncertainties, due to identification of individual velocity components (Fig. 7). Only for small inclination angles (i.e. clouds mostly in the plane of sky), accreted material at low column densities will display metallicities (given our model parameters) lower by more than 1 dex compared to the bulk of the cloud.

(v) The correlation between metallicities and column densities along a range of sightlines not only indicates mixing (Collins et al. 2007), but also could indicate the evolutionary stage of the cloud.

## ACKNOWLEDGEMENTS

We thank the anonymous referee for a focused and thoughtful report. This work was partially supported by *HST* grant no. *HST*-GO-13840.008-A, and by UNC Chapel Hill. It has made use of NASA's Astrophysics Data System. Special thanks to the PSI2/Interstellar Institute Programs at Université Paris-Saclay in 2017–2020. The authors thank B. Wakker and F. J. Lockman for detailed comments on (earlier versions of) the manuscript. Simulations were run on the UNC clusters *longleaf* and *dogwood*, administered by UNC's Information and Technology Services.

## DATA AVAILABILITY STATEMENT

Raw and reduced simulation data are available on request.

## REFERENCES

- Armillotta L., Fraternali F., Marinacci F., 2016, *MNRAS*, 462, 4157
- Armillotta L., Fraternali F., Werk J. K., Prochaska J. X., Marinacci F., 2017, *MNRAS*, 470, 114
- Benjamin R. A., Danly L., 1997, *ApJ*, 481, 764
- Bland-Hawthorn J., Veilleux S., Cecil G. N., Putman M. E., Gibson B. K., Maloney P. R., 1998, *MNRAS*, 299, 611
- Brüggen M., Scannapieco E., 2016, *ApJ*, 822, 31
- Brüns C., Kerp J., Pagels A., 2001, *A&A*, 370, L26
- Bryan G. L. et al., 2014, *ApJS*, 211, 19
- Chandrasekhar S., 1961, *Hydrodynamic and Hydromagnetic Stability*. International Series of Monographs on Physics. Clarendon, Oxford
- Collins J. A., Shull J. M., Giroux M. L., 2003, *ApJ*, 585, 336
- Collins J. A., Shull J. M., Giroux M. L., 2007, *ApJ*, 657, 271
- Cooper J. L., Bicknell G. V., Sutherland R. S., Bland-Hawthorn J., 2008, *ApJ*, 674, 157
- Cooper J. L., Bicknell G. V., Sutherland R. S., Bland-Hawthorn J., 2009, *ApJ*, 703, 330
- Cox D. P., 2005, *ARA&A*, 43, 337
- Di Teodoro E. M., McClure-Griffiths N. M., Lockman F. J., Denbo S. R., Endsley R., Ford H. A., Harrington K., 2018, *ApJ*, 855, 33
- Esquivel A., Benjamin R. A., Lazarian A., Cho J., Leitner S. N., 2006, *ApJ*, 648, 1043
- Ferrière K. M., 2001, *Rev. Mod. Phys.*, 73, 1031
- Field G. B., 1965, *ApJ*, 142, 531
- Forbes J. C., Lin D. N. C., 2019, *AJ*, 158, 124
- Fox A. J. et al., 2016, *ApJ*, 816, L11
- Fox A. J., Savage B. D., Wakker B. P., Richter P., Sembach K. R., Tripp T. M., 2004, *ApJ*, 602, 738
- Fox A. J., Wakker B. P., Smoker J. V., Richter P., Savage B. D., Sembach K. R., 2010, *ApJ*, 718, 1046
- Fraternali F., Marasco A., Armillotta L., Marinacci F., 2015, *MNRAS*, 447, L70
- Frazer C. C., Heitsch F., 2019, *MNRAS*, 489, 52

- Galyardt J., Shelton R. L., 2016, *ApJ*, 816, L18
- Gazol A., Vázquez-Semadeni E., Sánchez-Salcedo F. J., Scalo J., 2001, *ApJ*, 557, L121
- Girichidis P. et al., 2016, *ApJ*, 816, L19
- Gnat O., 2017, *ApJS*, 228, 11
- Gnat O., Sternberg A., McKee C. F., 2010, *ApJ*, 718, 1315
- Goodson M. D., Luebbers I., Heitsch F., Frazer C. C., 2016, *MNRAS*, 462, 2777
- Goodson M. D., Heitsch F., Eklund K., Williams V. A., 2017, *MNRAS*, 468, 3184
- Gottlieb S., Shu C. W., 1998, *Math. Comput.*, 67, 73
- Gritton J. A., Shelton R. L., Kwak K., 2014, *ApJ*, 795, 99
- Gritton J. A., Shelton R. L., Galyardt J. E., 2017, *ApJ*, 842, 102
- Gronke M., Oh S. P., 2020, *MNRAS*, 492, 1970
- Grønnow A., Tepper-García T., Bland-Hawthorn J., McClure-Griffiths N. M., 2017, *ApJ*, 845, 69
- Grønnow A., Tepper-García T., Bland-Hawthorn J., 2018, *ApJ*, 865, 64
- Gupta A., Mathur S., Krongold Y., Nicastro F., Galeazzi M., 2012, *ApJ*, 756, L8
- Heitsch F., Putman M. E., 2009, *ApJ*, 698, 1485
- Heitsch F., Bartell B., Clark S. E., Peek J. E. G., Cheng D., Putman M., 2016, *MNRAS*, 462, L46
- Henley D. B., Shelton R. L., 2014, *ApJ*, 784, 54
- Henley D. B., Gritton J. A., Shelton R. L., 2017, *ApJ*, 837, 82
- Hulsbosch A. N. M., Raimond E., 1966, *Bull. Astron. Inst. Netherlands*, 18, 413
- Ji S., Oh S. P., McCourt M., 2018, *MNRAS*, 476, 852
- Kooij R., Grønnow A., Fraternali F., 2021, *MNRAS*, 502, 1263
- Kwak K., Shelton R. L., 2010, *ApJ*, 719, 523
- Kwak K., Henley D. B., Shelton R. L., 2011, *ApJ*, 739, 30
- Kwak K., Shelton R. L., Henley D. B., 2015, *ApJ*, 812, 111
- Lehner N., Howk J. C., 2011, *Science*, 334, 955
- Lockman F. J., Benjamin R. A., Heroux A. J., Langston G. I., 2008, *ApJ*, 679, L21
- Lockman F. J., Di Teodoro E. M., McClure-Griffiths N. M., 2020, *ApJ*, 888, 51
- Marasco A., Fraternali F., 2017, *MNRAS*, 464, L100
- Marchal A., Miville-Deschênes M.-A., Orioux F., Gac N., Soussen C., Lesot M.-J., d'Allonnes A. R., Salomé Q., 2019, *A&A*, 626, A101
- Marinacci F., Binney J., Fraternali F., Nipoti C., Ciotti L., Londrillo P., 2010, *MNRAS*, 404, 1464
- McCourt M., O'Leary R. M., Madigan A.-M., Quataert E., 2015, *MNRAS*, 449, 2
- Miller M. J., Bregman J. N., 2013, *ApJ*, 770, 118
- Miller M. J., Bregman J. N., 2015, *ApJ*, 800, 14
- Murray C. E., Stanimirović S., Goss W. M., Heiles C., Dickey J. M., Babler B., Kim C.-G., 2018, *ApJS*, 238, 14
- Nichols M., Bland-Hawthorn J., 2009, *ApJ*, 707, 1642
- Nichols M., Colless J., Colless M., Bland-Hawthorn J., 2011, *ApJ*, 742, 110
- Nichols M., Mirabal N., Agertz O., Lockman F. J., Bland-Hawthorn J., 2014, *MNRAS*, 442, 2883
- Peek J. E. G., Putman M. E., McKee C. F., Heiles C., Stanimirović S., 2007, *ApJ*, 656, 907
- Pittard J. M., Parkin E. R., 2016, *MNRAS*, 457, 4470
- Putman M. E. et al., 2002, *AJ*, 123, 873
- Putman M. E., Bland-Hawthorn J., Veilleux S., Gibson B. K., Freeman K. C., Maloney P. R., 2003, *ApJ*, 597, 948
- Putman M. E., Peek J. E. G., Joungh M. R., 2012, *ARA&A*, 50, 491
- Qu Z., Bregman J. N., Hodges-Kluck E., Li J.-T., Lindley R., 2020, *ApJ*, 894, 142
- Quilis V., Moore B., 2001, *ApJ*, 555, L95
- Richter P., 2017, in Fox A., Dav'e R., eds, *Astrophysics and Space Science Library* Vol. 430, Gas Accretion onto Galaxies. Springer, Heidelberg, p. 15
- Richter P., Sembach K. R., Wakker B. P., Savage B. D., Tripp T. M., Murphy E. M., Kalberla P. M. W., Jenkins E. B., 2001, *ApJ*, 559, 318
- Richter P., Fox A. J., Wakker B. P., Lehner N., Howk J. C., Bland-Hawthorn J., Ben Bekhti N., Fechner C., 2013, *ApJ*, 772, 111
- Sander B., Hensler G., 2021, *MNRAS*, 501, 5330
- Shin M., Stone J. M., Snyder G. F., 2008, *ApJ*, 680, 336
- Shull J. M., Moss J. A., 2020, *ApJ*, 903, 101
- Shull J. M., Jones J. R., Danforth C. W., Collins J. A., 2009, *ApJ*, 699, 754
- Shull J. M., Stevans M., Danforth C., Penton S. V., Lockman F. J., Arav N., 2011, *ApJ*, 739, 105
- Shull J. M., Danforth C. W., Anderson K. L., 2021, *ApJ*, 911, 55
- Smith G. P., 1963, *Bull. Astron. Inst. Netherlands*, 17, 203
- Spitzer L., 1962, *Physics of Fully Ionized Gases*, Interscience Publishers, New York
- Stone J. M., Gardiner T., 2007, *ApJ*, 671, 1726
- Stone J. M., Zweibel E. G., 2009, *ApJ*, 696, 233
- Stone J. M., Gardiner T. A., Teuben P., Hawley J. F., Simon J. B., 2008, *ApJS*, 178, 137
- Strickland D. K., Stevens I. R., 2000, *MNRAS*, 314, 511
- Sutherland R. S., Dopita M. A., 1993, *ApJS*, 88, 253
- Tanner R., Cecil G., Heitsch F., 2016, *ApJ*, 821, 7
- Thom C., Peek J. E. G., Putman M. E., Heiles C., Peek K. M. G., Wilhelm R., 2008, *ApJ*, 684, 364
- Toro E. F., Spruce M., Speares W., 1994, *Shock Waves*, 4, 25
- Tripp T. M. et al., 2003, *AJ*, 125, 3122
- Vieser W., Hensler G., 2007a, *A&A*, 472, 141
- Vieser W., Hensler G., 2007b, *A&A*, 475, 251
- Vietri M., Ferrara A., Miniati F., 1997, *ApJ*, 483, 262
- Wakker B. P. et al., 1999b, *Nature*, 402, 388
- Wakker B. P. et al., 2003, *ApJS*, 146, 1
- Wakker B. P. et al., 2007, *ApJ*, 670, L113
- Wakker B. P., van Woerden H., 1997, *ARA&A*, 35, 217
- Wakker B. P., Savage B. D., Oosterloo T. A., Putman M. E., 1999a, in Gibson B. K., Putman M. E., eds, *ASP Conf. Ser. Vol. 166, Stromlo Workshop on High-Velocity Clouds*. Astron. Soc. Pac., San Francisco, p. 302
- Wakker B. P., Kalberla P. M. W., van Woerden H., de Boer K. S., Putman M. E., 2001, *ApJS*, 136, 537
- Wakker B. P., Lockman F. J., Brown J. M., 2011, *ApJ*, 728, 159
- Wang Q. D., Yao Y., 2012, preprint ([arXiv:1211.4834](https://arxiv.org/abs/1211.4834))
- Wolfire M. G., Hollenbach D., McKee C. F., Tielens A. G. G. M., Bakes E. L. O., 1995a, *ApJ*, 443, 152
- Wolfire M. G., McKee C. F., Hollenbach D., Tielens A. G. G. M., 1995b, *ApJ*, 453, 673
- Zhu C., Byrd R. H., Lu P., Nocedal J., 1997, *ACM Trans. Math. Softw.*, 23, 550

## APPENDIX A: MODIFICATIONS TO ATHENA

The code is available at FH's [github](#) repository. The initialization file can be found under `src/prob/fheitsch/hvc.c`.

### A1 PPV Cubes

Because of the high resolution requirements, we implemented an on-the-fly analysis, including the calculation of position–position–velocity (PPV) cubes for selected viewing angles. All lines-of-sight can be calculated at initialization of the simulation. The block decomposition used in the parallelization requires that each processor dumps its version of a rotated PPV cube. These are then added and stitched together in a post-processing step. This approach limits the radiative transfer to optically thin emission and/or background absorption. Self-absorption cannot be modelled. We calculate spectra for two species.

The H I-21 cm emission is determined for each velocity channel  $v$  as the integral along the line of sight  $s$ ,

$$T_b(v) = c_{\text{HI}}^{-1} \int n(s) \phi(v - v(s)) ds, \quad (\text{A1})$$



where  $n(s)$  is the local density in  $\text{cm}^{-3}$  along the line of sight for gas with  $T < 10^4$  K, and the function

$$\phi(v - v(s)) = \frac{1}{\sqrt{\pi} \Delta v_{\text{th}}(s)} \exp \left( - \left( \frac{v - v(s)}{\Delta v_{\text{th}}(s)} \right)^2 \right) \quad (\text{A2})$$

describes the thermal broadening with the local thermal width  $\Delta v_{\text{th}}(s) = \sqrt{2k_B T(s)/m_H}$ , where  $m_H$  is the hydrogen atom mass, and  $k_B$  the Boltzmann constant. The constant  $c_{\text{HI}} = 1.823 \times 10^{18} \text{ cm}^{-2} (\text{K km s}^{-1})^{-1}$ . Each channel is  $\Delta v = 1 \text{ km s}^{-1}$  wide. The brightness temperature can be converted into a total column density via

$$N(\text{HI}) = c_{\text{HI}} \int T_b(v) dv. \quad (\text{A3})$$

The absorption by a tracer species (for example singly ionized sulphur, S II, Fox et al. 2016) is calculated based on the local metallicity,

$$Z = Z_c C_c + Z_h C_h, \quad (\text{A4})$$

where the subscripts  $c/h$  denote cloud/halo material, and with the sum of the ‘colour’ fields identifying cloud and halo material,  $C_c + C_h = 1$ . The colour field for the cloud  $C_c$  is defined via equation (7). We write the absorption coefficient as

$$\kappa(s) = \sigma_{\text{SII}} Z(s) n(s), \quad (\text{A5})$$

assuming  $\sigma_{\text{SII}} = 10^{-22} \text{ cm}^2$  as a cross-section for the tracer. The exact choice is irrelevant for our purposes, and is solely motivated by rendering the resulting absorption line as optically thin, i.e. the optical depth at a given velocity channel  $v$  is given by

$$\tau(v) = \int \kappa(s) \phi(v - v(s)) ds. \quad (\text{A6})$$

The column density per channel  $N(v)$  can then be calculated as  $\tau(v)/\sigma_{\text{SII}}$ . We note that we use the same mean molecular weight for H I and the tracer species. Further, we neglect any issues arising from varying ionization degrees (Fox et al. 2016). In that sense, our ‘metal absorber’ is just a generic quantity, providing the simplest possible model. The closest equivalent to observational measurements would be metallicity estimates via O I/H I coupled via charge exchange (Collins et al. 2003).

## A2 Internal energy

The Athena stock version applies density and pressure floors after the reconstruction step as a safeguard to prevent negative densities and/or pressures in extreme flow situations. For problems involving radiative losses, the floor values can lead to unreasonably high heating rates, leading to point-wise ‘explosions’. Therefore, we implemented an internal energy integration following Bryan et al. (2014). Details are discussed by Goodson et al. (2016) and Frazer & Heitsch (2019).

## A3 Time stepping

To increase the stability of the code in the presence of strong temperature gradients and high-Mach number shocks, we implemented a time-variation-diminishing third-order Runge–Kutta integrator (Gottlieb & Shu 1998) in Athena. While slower than the CTU and VL integrators of the Athena 4.2 stock version, the benefit of improved stability while being able to run at Courant numbers of 0.5 seemed a reasonable trade-off. The RK3 architecture has the advantage that arbitrary source terms can be included with ease at third order in time, i.e. at the same order as the hydrodynamical fluxes. This is especially

of advantage in the case of energy source terms such as cooling (Section A4) or co-moving grids (Section A5). Despite the higher time-accuracy, extreme flow situations, specifically in the presence of radiative losses, can occasionally lead to negative densities. In such cases, the integrator repeats the failed step at half the Courant time-step for the whole grid.

## A4 Thermal physics

Heating and radiative losses are implemented as a look-up table in five variables, namely the gas density  $n$ , the temperature  $T$ , the distance from the Galactic plane  $z$  to account for reduction of soft UV radiation density, the column density  $N$  to account for UV and x-ray shielding, and the metallicity  $Z$ . Tables were generated with Mappings-V (Sutherland & Dopita 1993). The  $z$ -dependence of the radiation field follows Wolfire et al. (1995b). Fig. A1 shows the thermal equilibrium pressures  $P$ , temperatures  $T$ , and ionization degrees against gas density  $n$ , in dependence of metallicity (left), distance above the plane (center), and shielding column (right). Metallicity and shielding can strongly affect the thermal behaviour of the gas (Wolfire et al. 1995b). The calculation of the ionization degree assumes collisional ionization equilibrium, since we are interested only in the overall dynamics rather than the details of the turbulent mixing layers or the ionization stages of various ions (Kwak & Shelton 2010; Gnat, Sternberg & McKee 2010). We use the ionization degree to determine the fraction of neutral gas during the analysis step. A detailed treatment of the thermal physics across ‘phase transitions’ (e.g. Stone & Zweibel 2009) including non-equilibrium cooling can change the nature of the transition and thus could eventually affect the efficiency of ambient gas condensation in the cloud wake (Gnat 2017).

Heating and cooling are implemented as sources  $\dot{E}_{\text{cool}}$  to the total energy equation,

$$\partial_t E + \nabla \cdot (\mathbf{u}(E + P)) = \dot{E}_{\text{cool}}. \quad (\text{A7})$$

To prevent overshoots once thermal equilibrium is reached, and to avoid negative temperatures, we sub-cycle on the cooling using an adaptive stepsize Runge–Kutta–Fehlberg integrator, solving

$$\frac{dT}{dt} = f(n, T, N, Z, z). \quad (\text{A8})$$

The RKF integrator subcycles on equation (A8) until a full Courant time-step  $\Delta t$  is reached. The resulting energy difference  $\Delta E$  is used to calculate

$$\dot{E}_{\text{cool}} = \frac{\Delta E}{\Delta t}. \quad (\text{A9})$$

## A5 Comoving grid

There are two advantages to have the simulation domain track the cloud. First, we can limit the simulation domain to a box around the cloud. This allows us to track the cloud for an arbitrary amount of time, as long as we provide the correct (time- and position-dependent) boundary conditions. Gritton et al. (2014) and Galyardt & Shelton (2016) decided to solve this problem by using adaptive mesh refinement in a domain spanning the whole trajectory of the cloud, refining only on the position of the cloud. Yet, since we are mostly interested in turbulent mixing, we decided to insist on a uniform spatial resolution. Shin et al. (2008) point out the second advantage, namely that a comoving grid can be realized by subtracting the centre-of-mass velocity from the box, thus reducing the effect of truncation errors in the cloud dynamics. We follow their approach, adjusting



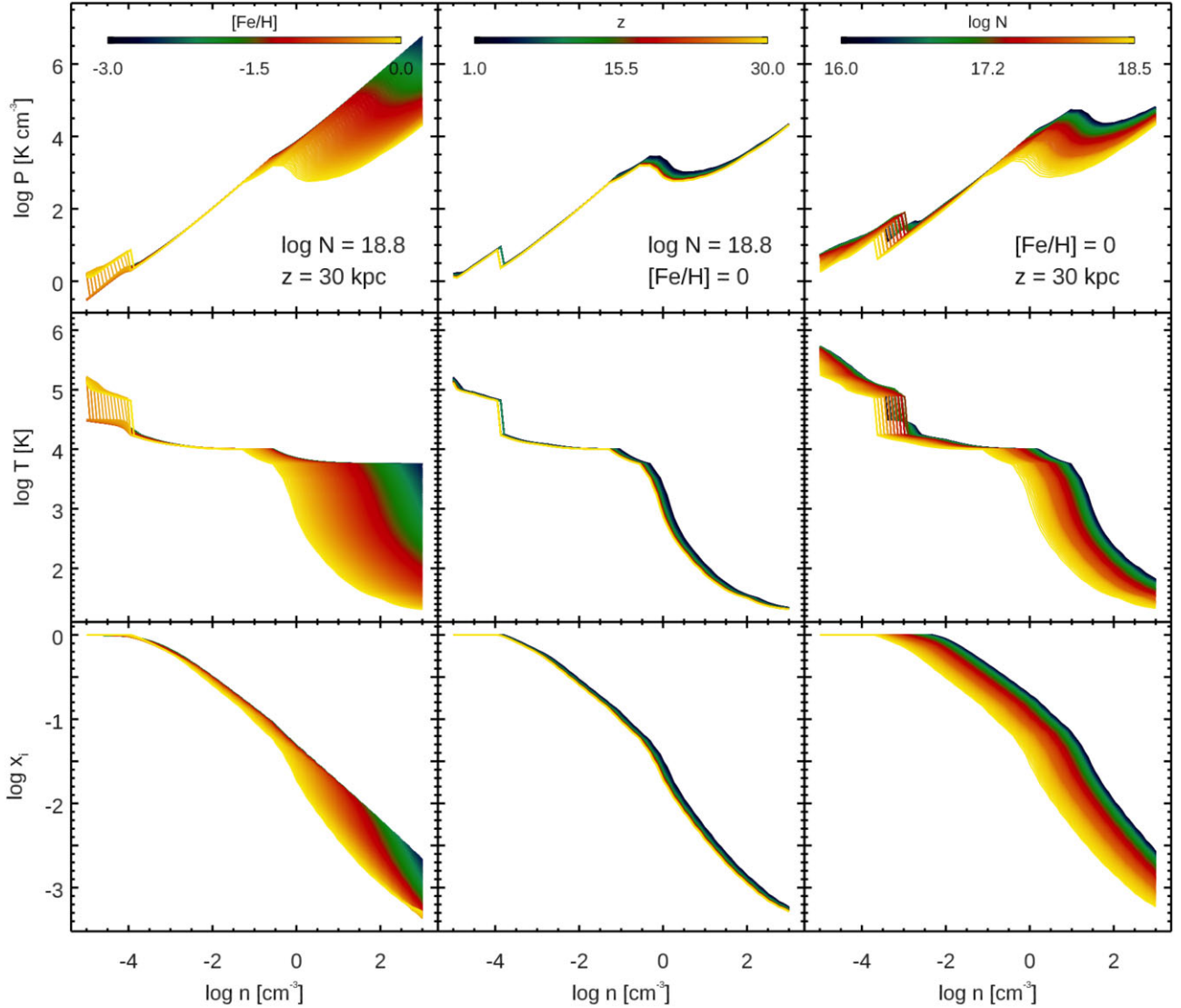


**Figure A1.** Thermal equilibrium pressure (top), temperature (center), and ionization fraction (bottom) against density, in dependence of metallicity (left), distance from plane (center), and shielding column (right). Metallicity and shielding column have the strongest effect on the thermal behaviour of the gas. The ionization fraction is used to calculate the amount of neutral H I.

the subtracted velocity such that the leading cloud edge is kept at a (nearly) constant position within the box (see also Goodson et al. 2017). The comoving grid is implemented as a change in position and velocity applied to the grid coordinates, updated together with the fluid variables. Thus, the grid positions are updated together with the RK3 integration. The RK3 integrator takes care of resetting the coordinates also, in case a time-step needs to be repeated (see Appendix A3).

## APPENDIX B: ROHSA

Fitting the spectra to determine column densities and thus abundances met with two challenges. First, a single position–position–velocity cube can contain thousands of usable lines of sight, since we are not limited to background sources for absorption spectra. Secondly, a single line of sight may contain multiple velocity components, the number of which is not known in advance. The first challenge mandates a fast and efficient fitting mechanism, and the second challenge requires the fitting procedure to allow for an arbitrary

number of Gaussian components, yet ideally without overfitting the data. We use a modified version of ROHSA (Marchal et al. 2019) that decomposes jointly the emission and absorption position–position–velocity cubes described in Appendix A1 into multiple velocity components using a Gaussian model.

## B1 Model

The data are the measured brightness temperature  $T_b(v, \mathbf{r})$  and optical depth  $\tau(v, \mathbf{r})$  at a given projected velocity  $v$ . The proposed model  $\tilde{T}_b(v, \boldsymbol{\theta}^{em}(\mathbf{r}))$  and  $\tilde{\tau}(v, \boldsymbol{\theta}^{\tau}(\mathbf{r}))$  are a sum of  $N$  Gaussian  $G(v, \boldsymbol{\theta}_n(\mathbf{r}))$

$$\tilde{T}_b(v, \boldsymbol{\theta}^{em}(\mathbf{r})) = \sum_{n=1}^N G(v, \boldsymbol{\theta}_n^{em}(\mathbf{r})), \quad (\text{B1})$$

$$\tilde{\tau}(v, \boldsymbol{\theta}^{\tau}(\mathbf{r})) = \sum_{n=1}^N G(v, \boldsymbol{\theta}_n^{\tau}(\mathbf{r})), \quad (\text{B2})$$

with  $\theta^{em}(\mathbf{r}) = (\theta_1^{em}(\mathbf{r}), \dots, \theta_n^{em}(\mathbf{r}))$ ,  $\theta^\tau(\mathbf{r}) = (\theta_1^\tau(\mathbf{r}), \dots, \theta_n^\tau(\mathbf{r}))$ , and where

$$G(v, \theta_n(\mathbf{r})) = a_n(\mathbf{r}) \exp\left(-\frac{(v - \mu_n(\mathbf{r}))^2}{2\sigma_n(\mathbf{r})^2}\right) \quad (\text{B3})$$

is parametrized by  $\theta_n = (a_n, \mu_n, \sigma_n)$  with  $a_n \geq 0$  being the amplitude,  $\mu_n$  the position, and  $\sigma_n$  the standard deviation 2D maps of the  $n$ th Gaussian profile. The residuals are

$$L^{em}(v, \theta^{em}(\mathbf{r})) = \tilde{T}_b(v, \theta^{em}(\mathbf{r})) - T_b(v, \mathbf{r}), \quad (\text{B4})$$

and

$$L^\tau(v, \theta^\tau(\mathbf{r})) = \tilde{\tau}(v, \theta^\tau(\mathbf{r})) - \tau(v, \mathbf{r}). \quad (\text{B5})$$

The estimated parameters  $\hat{\theta}^{em}$  and  $\hat{\theta}^\tau$  are defined as the minimizer of a cost function that includes the sum of the squares of the residuals,

$$Q(\theta^{em}, \theta^\tau) = \frac{1}{2} \lambda_{em} \|L^{em}(v, \theta^{em})\|_2^2 + \frac{1}{2} \lambda_\tau \|L^\tau(v, \theta^\tau)\|_2^2, \quad (\text{B6})$$

where,  $\lambda_{em}$ , and  $\lambda_\tau$  are hyperparameters than tune the balance between the emission and absorption terms. Although the two terms in equation (B6) are combined in a single cost function, the parameters  $\theta^{em}$  and  $\theta^\tau$  are independent and the estimated parameters obtained using any arbitrary optimization algorithm would lead to the same result as if they were evaluated separately. However, such a combination allows us to add regularization terms as priors on the model parameters  $\theta^{em}$  and  $\theta^\tau$ .

Following Marchal et al. (2019), each parameter map of  $\theta^{em}(\mathbf{r})$  and  $\theta^\tau(\mathbf{r})$  is filtered using a Laplacian kernel to ensure that the solution is spatial coherent. In other words, adjacent pixels are forced to have a similar Gaussian decomposition. The following regularization term, itself containing energy terms, is added to the cost function given in equation (B6)

$$R(\theta^{em}, \theta^\tau) = \frac{1}{2} \sum_{n=1}^N \lambda_a^{em} \|D a_n^{em}\|_2^2 + \lambda_\mu^{em} \|D \mu_n^{em}\|_2^2 \quad (\text{B7})$$

$$+ \lambda_\sigma^\tau \|D \sigma_n^\tau\|_2^2 \quad (\text{B8})$$

$$+ \frac{1}{2} \sum_{n=1}^N \lambda_a^\tau \|D a_n^\tau\|_2^2 + \lambda_\mu^\tau \|D \mu_n^\tau\|_2^2 \quad (\text{B9})$$

$$+ \lambda_\sigma^\tau \|D \sigma_n^\tau\|_2^2, \quad (\text{B10})$$

where  $D$  is the matrix perform the 2D convolution (see Marchal et al. 2019 for complementary details), and  $\lambda_a^{em}$ ,  $\lambda_\mu^{em}$ ,  $\lambda_\sigma^{em}$ ,  $\lambda_a^\tau$ ,  $\lambda_\mu^\tau$ ,  $\lambda_\sigma^\tau$  are hyperparameters than tune the balance between the different terms.

In addition, we also add the following regularization term to the cost function given in equation (B6)

$$R'(\theta^{em}, \theta^\tau) = \frac{1}{2} \sum_{n=1}^N \lambda_\mu \| \mu_n^{em} / \mu_n^\tau - 1 \|_2^2 + \lambda_\sigma \| \sigma_n^{em} / \sigma_n^\tau - 1 \|_2^2, \quad (\text{B11})$$

where  $\lambda_\mu$  and  $\lambda_\sigma$  are hyperparameters than tune the balance between the different terms. These energy terms aim to maximize the corre-

lation of the velocity fields and dispersion velocity fields between emission and absorption. In other words, these energy terms ensure that each Gaussian pair describing a component seen in absorption and emission has a similar velocity and a similar velocity dispersion.

The full cost function is then

$$J(\theta^{em}, \theta^\tau) = Q(\theta^{em}, \theta^\tau) + R(\theta^{em}, \theta^\tau) + R'(\theta^{em}, \theta^\tau), \quad (\text{B12})$$

and the minimizer is

$$[\hat{\theta}^{em}, \hat{\theta}^\tau] = \operatorname{argmin} J(\theta^{em}, \theta^\tau), \quad (\text{B13})$$

wrt.  $a_n^{em} \geq 0, \sigma_n^\tau \geq 0 \forall n \in [1, \dots, N]$ . Following Marchal et al. (2019), this optimization relies on L-BFGS-B (for Limited-memory Broyden–Fletcher–Goldfarb–Shanno with Bounds), a quasi-Newton iterative algorithm described by Zhu et al. (1997) that allows for the positivity constraints of the amplitudes to be taken into account.

The initialization of the optimization is carried out in two steps. First, the optical depth model  $\theta^\tau$  is adjusted using the second term in equation (B6). For this step, we use the multiresolution process from coarse to fine grid described in Marchal et al. (2019). Then the solution  $\theta^\tau$  is used to initialize  $\theta^{em}$ . Finally, the full cost function given in equation (B12) is used to perform the final optimization and to update  $\theta^\tau$  and  $\theta^{em}$ , ensuring a spatially coherent solution with a correlated velocity field and velocity dispersion field for each Gaussian component.

The decomposition is performed using ROHSA hyperparameters  $N=6$ , and  $\lambda_{em} = \lambda_\tau = \lambda_a^{em} = \lambda_\mu^{em} = \lambda_\sigma^{em} = \lambda_a^\tau = \lambda_\mu^\tau = \lambda_\sigma^\tau = 1$ . The number of Gaussian  $N$  is chosen to ensure that the signal is fully encoded. Note that due to regularization, this does not imply that six Gaussians are used along each line of sight (Marchal et al. 2019).

## B2 Estimating physical parameters

The spatially coherent parameters  $\hat{\theta}^{em}, \hat{\theta}^\tau$  obtained with ROHSA allows us to extract the mean physical properties of the HVC gas along each line of sight.

The column density map is

$$N(\text{HI})(\mathbf{r}) = C a_n^{em}(\mathbf{r}) \sigma_n^{em}(\mathbf{r}). \quad (\text{B14})$$

All the following quantities (metallicity, centroid velocity, and total velocity dispersion, see also equations 11 and 10) are weighted, by the column density,

$$\bar{Z}(\mathbf{r}) = \frac{\sum_{n=1}^N N(\text{HI})_n(\mathbf{r}) (a_n^\tau(\mathbf{r}) / a_n^{em}(\mathbf{r}))}{\sum_{n=1}^N N(\text{HI})_n(\mathbf{r})}, \quad (\text{B15})$$

$$v_c = \frac{\sum_v v \tilde{T}_b(\mathbf{r})}{\sum_v \tilde{T}_b(\mathbf{r})}, \quad (\text{B16})$$

$$\bar{\sigma}^2(\mathbf{r}) = \frac{\sum_v (v - v_c(\mathbf{r}))^2 \tilde{T}_b(\mathbf{r})}{\sum_v \tilde{T}_b(\mathbf{r})}. \quad (\text{B17})$$

This paper has been typeset from a  $\text{\LaTeX}$  file prepared by the author.